Royal Netherlands
Meteorological Institute
Ministry of Infrastructure and the Environment

TROPOMI's Aerosol Layer Height Algorithm: interpretation of the retrieved height parameter

C.E. Koning

KNMI Internal report IR-2014-02

VRIJE UNIVERSITEIT AMSTERDAM

MASTER'S THESIS

April 2014

TROPOMI's Aerosol Layer Height Algorithm: Interpretation of the retrieved height parameter

---

Author:
C.E. Koning

Supervisors:
A.F.J. Sanders (KNMI)
A.C.M. Ran (VU)

Vrije Universiteit Amsterdam
Faculteit der Exacte
Wetenschappen
De Boelelaan 1081a
1081 HV Amsterdam

Koninklijk Nederlands
Meteorologisch Insituut
Aardobservatie Klimaat
Utrechtseweg 297
3731 GA De Bilt

VU VRIJE UNIVERSITEIT AMSTERDAM

Royal Netherlands
Meteorological Institute
Ministry of Infrastructure and the Environment

Preface

This is the Master's thesis for my Master in Mathematics at the Vrije Universiteit Amsterdam (VU). The research presented here was conducted in the form of a research internship at Koninklijk Nederlands Meteorologisch Instituut (KNMI). This thesis also functions as the final report for the internship.

At KNMI, I worked in the division of Climate Observations. In this division, I specifically worked within the TROPOMI algorithm team. This team develops algorithms for TROPOMI, which is ESA's Sentinel-5 precursor mission's measuring instrument. Within the TROPOMI algorithm team, I conducted research on the Aerosol Layer Height algorithm under the supervision of Bram Sanders.

The role of supervisor from the VU was fulfilled by André Ran. The second reader of this thesis is Joost Hulshof. Both are professors of mathematics at the Faculty of Exact Sciences of the VU.

First, and foremost, I want to thank Bram Sanders. For supporting my research throughout all of its ups and downs. For the enormous amounts of effort he has put in my supervision. For allowing me to work on, as how I like to put it, *his* algorithm. And for being a great supervisor in general.

Others from KNMI that deserve praise are Johan de Haan, Arnoud Apituley, Piet Stammes, Erwin Loots and Maarten Sneep for their support, feedback and discussions. Of course, the rest of the Earth Observation and Climate department also deserve thanks for their support, for their hospitality, and because they have made it possible, and pleasant, for me to work at KNMI.

From the VU I would like to thank André Ran for giving me the necessary mathematical guidance. I also want to express my appreciation for Joost Hulshof, for being the second reader of this thesis. Additionally, I want to thank Mathisca de Gunst, for some statistical discussion which, sadly, did not make it into this thesis; Annemieke van Goor, for her counseling during my search for an internship; and Corrie Quant for her counseling throughout my entire academic career.

Last, but not least, I want to thank my family and friends for their unending support, but also for their attempts at distraction.

Writing this thesis has turned out to be a very demanding task. A large amount of effort has been put into making everything just right and I hope that it shows.

I hope you find this thesis to be an interesting read.

Casper Koning
April 22th 2014
Utrecht

Abstract

TROPOMI's Aerosol Layer Height algorithm currently assumes a simplified aerosol profile in the form of a single layer of homogeneously distributed aerosols. The height of this layer is retrieved by using height information from the O_2 A band. It is not straightforward to interpret the retrieved height parameter, since true aerosol profiles are typically complex and heterogeneous.

We used radiative transfer theory to better understand the retrieved parameter. In addition to an available multiple scattering description of the radiation field, a single scattering approximation was developed as well. Comparing the single scattering approximation to the full multiple scattering radiative transfer revealed that the approximation is accurate inside strong absorption parts of the O_2 A band for realistic aerosol profiles.

Retrieval simulations for realistic aerosol scenes suggested that the retrieved height parameter can be interpreted as a centroid of the aerosol profile, if the surface albedo is not fitted.

The retrieved height parameter was compared to three different centroids of the aerosol extinction profile, which are constructed using weighted averages. Two of these methods take into account the sensitivity of the measured top of atmosphere radiance with respect to aerosol at different altitudes. This sensitivity was obtained by taking a directional derivative of a functional, which maps the aerosol extinction profile to a measured top of atmosphere radiance. This yields semi-analytic derivatives. The two methods differ in the way the derivatives are determined. The first uses a multiple scattering description and the other uses the single scattering approximation. All centroid methods showed good agreement with the retrieved height parameter.

In additional retrieval experiments we also fitted the surface albedo. These experiments showed that, as soon as the standard error of the surface albedo exceeds 10^{-3}, a bifurcation occurs, which results in unrealistic results. These unrealistic results can no longer be interpreted as centroids of aerosol extinction profiles.

Contents

Chapter 1

Introduction

Aerosols are tiny solid particles or droplets suspended in the atmosphere, e.g. dust, soot, volcanic ash and air pollutants. They are typically smaller than a micrometer. Aerosols are interesting in many different fields, like climate studies, meteorological models, remote sensing and air quality.

In the Earth's radiation balance, aerosols play a large role. Aerosols can cool the atmosphere by scattering radiation outwards. They can affect the radiation by locally warming the atmosphere through absorption. Furthermore, they play an important role in cloud formation, as they often function as cloud forming nuclei. Therefore, they play a fundamental role in climate and meteorology. For the same reasons, they are also a key parameter in the inversion of satellite data, as they affect the radiation measured at the top of the atmosphere.

Furthermore, aerosols are a large subset of the Earth's air pollutants. The World Health Organization recently reported that in 2012 around 7 million people died as a result of air pollution exposure, see [1]. This means that air pollution is the world's largest single environmental health risk.

Because of the volcanic ash that was injected into the atmosphere during the eruption of the Icelandic volcano Eyjafjallajökull between April and May 2010, a large part of Europe's air space was closed for over six days. The International Air Transport Association reports that the loss due to this event totals over \$2.5 billion, see [2]. Maybe, if we had known the vertical distribution of the aerosol, we could have allowed the aircrafts to fly at different altitudes, avoiding the aerosol. This vertical distribution was indeed investigated later, see [3].

Various techniques are being developed to obtain information on the vertical distribution of aerosols. Lidar is a remote sensing technology that measures atmospheric composition by measuring the backscattered light of a narrow laser beam. By repeatedly sending out laser pulses one can obtain information about the vertical structure of the atmosphere. This technology is used extensively to obtain detailed knowledge of the vertical structure of aerosol. The European Aerosol Research Lidar Network (EARLINET, [4]) provides a network of ground-based lidars performing aerosol vertical distribution measurements. However, we can only obtain local information using these techniques. Because aerosol vertical distribution shows spatial variation and we are unable to obtain global coverage with ground-based lidars, there is a clear need for other methods.

The Cloud-Aerosol Lidar and Infrared Pathfinder Satellite Observation (CALIPSO) satellite is the first satellite to carry a lidar on-board dedicated to monitoring aerosol and cloud distribution from space. This novel method of monitoring aerosols has led the way to a large amount of new interesting research on the topic of aerosol distribution, e.g. [5]. However, the lidar on-board this satellite can still only obtain very localized data due to its narrow ground track.

Finally, methodologies are being developed to obtain information on the vertical distribution of aerosol from satellite measurements of sunlight reflected by the atmosphere. The spatial coverage of these methods is much larger than for methods based on lidar technology. One passive remote sensing technique is the Aerosol Layer Height algorithm, see [6] and [7]. This algorithm is being developed at KNMI for the Sentinel-5 Precursor mission's Tropospheric Monitoring Instrument (TROPOMI), see [8]. This spectrometer, jointly developed by The Netherlands and ESA, has daily global coverage with spectral bands in the ultraviolet, the visible, the near-infrared and the shortwave infrared. The Aerosol Layer Height algorithm exploits absorption of radiation in the O_2 A band in the near-infrared to obtain height information.

In the Earth's atmosphere, we observe numerous different cloud types. Take, for example, the thin high cirrus, the thick low stratocumulus, or the extremely large dense cumulonimbus clouds. Furthermore, several of these cloud species can be present at the same time. For aerosols, we observe similar behavior. Aerosols can be near the surface if they are close to their source, but they can also be elevated if they are emitted by a volcano or carried by wind. Furthermore, the structure of aerosol clouds can vary due to the various aerosol species that form these clouds. Thus, the vertical distribution of both clouds and aerosol is complex and can be very heterogeneous.

Due to the similarity of the retrieval problems, and the experience in cloud retrievals, aerosol research is often inspired by work already done for clouds. Operational cloud products typically assume a simplified cloud profile. A common parameterization is a single reflecting layer (e.g. [9], [10] and [11]). Building on the experiences with the cloud products, the Aerosol Layer Height algorithm also assumes a single layer. For this single layer of homogeneously distributed aerosol, atmospheric properties are fitted. Assuming such a simplified parameterization of a profile has consequences for the interpretation of the retrieval results, as there is a fundamental difference between the assumed layer and the actual profile. One immediately wonders how the retrieved height of a single layer relates to a (complex) true profile. Thus, research is needed to understand and interpret the retrieved height properly.

Experience has shown that the (operational) cloud products can often be interpreted as the centroid of a cloud profile. Aerosol Layer Height retrieval simulations suggest (see chapter 3) that we might interpret the Aerosol Layer Height as some centroid of an aerosol profile as well. Again, we turn to cloud retrievals to better understand this.

Knowledge of the light field in cloudy atmospheres can be used to gain a better understanding of retrieved cloud height. In [12], centroids of cloud profiles are derived by computing a particular weighted average of these cloud profiles. This weighted average takes into account properties of the light field for cloudy atmospheres (diffusion limit). These computed centroids can then be compared to operational (remote sensing) cloud products. Indeed, there is agreement between the computed centroids and the retrieved cloud heights of the cloud height products.

Since aerosol layers tend to be much less dense than cloud layers, their impact on the radiation field is significantly different from that of normal clouds. Thus, the weighted averaging scheme for cloud profiles is not appropriate for aerosol profiles. Instead, we turn back to radiative transfer to understand how aerosols impact the measured radiance. It seems suitable, see [13], that the single scattering of light is the most important effect for aerosols (single scattering limit).

Of course, the actual retrieved height parameter is the "true" centroid of a profile, and centroids based on simplified weighted averaging schemes may differ from this retrieved height. However, computing centroids from a simplified weighted averaging scheme has the advantage that it does not require complex radiative transfer computations. Furthermore, they can easily be computed for lidar measurements. This makes these methods ideal for large scale validation studies of the operational products (as seen in [12]).

In this thesis, we investigate how we should interpret retrieved Aerosol Layer Height from TROPOMI's Aerosol Layer Height algorithm. We also develop a single scattering approximation to the radiative transfer equation. Not only can this approximation be used to develop a simplified weighted averaging scheme for aerosol profiles, but it is also useful to better understand the radiation field for aerosol, which helps to further optimize the Aerosol Layer Height algorithm.

This thesis is structured as follows: First, we discuss how we can obtain aerosol height information from passive remote sensing observations in chapter 2. There, we also introduce the Aerosol Layer Height algorithm. In chapter 3, we construct realistic aerosol profiles for which we perform Aerosol Layer Height retrieval simulations. We introduce the radiative transfer equation and related concepts in chapters 4 and 5. Then, in chapter 6, we derive a single scattering approximation to the radiative transfer equation. For this approximation we derive an analytic solution, and semi-analytic derivatives, which we use for the construction of a weighted averaging scheme in chapter 7. Finally, in chapter 8, we perform additional retrieval experiments to investigate the effect of fitting the surface albedo as well. We conclude with a summary of our findings in chapter 9.

Chapter 2

Retrieving Aerosol Height

2.1 Physical Basis

When sunlight enters the atmosphere, photons get scattered and absorbed by atmospheric constituents, such as particles, trace gases, molecules and clouds. Of course, light also gets reflected by our planet's surface. Subsequently, after being exposed to these extinction processes, radiation can leave the atmosphere again. By carefully modeling the radiative transfer in the atmosphere, and comparing simulated top of atmosphere radiance signals against satellite measurements, we can retrieve atmospheric properties such as the height distribution of aerosol.

Throughout the light spectrum, the processes involved with extinction vary both qualitatively and quantitatively, and thus different processes may be used to obtain information about different quantities of interest. The Aerosol Layer Height algorithm exploits the absorption of radiation by oxygen in the A band (759 - 770 nm) to obtain height information for aerosol.

Consider an atmosphere with scattering aerosols between 900 and 800 hPa, or between 500 and 400 hPa. The measured spectra for these atmospheres are simulated in Figure 2.1. We clearly observe a decrease in absorption when the aerosol layer is more elevated.

When only considering single scattering (light that is scattered only once), the previous example can be explained as follows. Obviously, the more elevated aerosol layer reflects sunlight closer to the top of the atmosphere. Thus, a photon's path through the atmosphere is typically shorter, compared to light reflected by the lower layer. Because of the shorter path length, there is less absorption due to interaction with oxygen molecules, and a stronger radiance signal is observed inside the absorption band. Thus, there is information about the height distribution of aerosol inside the absorption band.

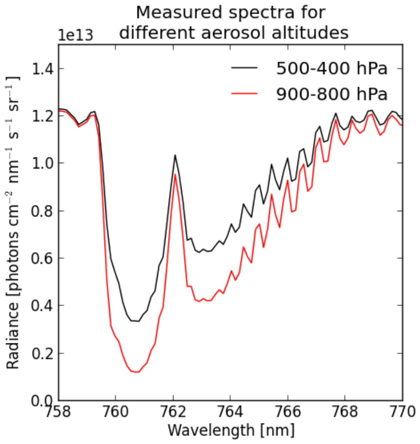

FIGURE 2.1: Simulated measured radiance spectra for an atmosphere with aerosol layers at different altitudes. The atmosphere with the high-altitude (low-pressure) aerosol layer yields a stronger radiance signal inside the absorption band, since light is typically reflected higher in the atmosphere and thus there is less absorption.

However, besides single scattering, many other complex processes influence the top of atmosphere radiance. For example, we also need to account for multiple scattering, aerosol absorption, and interactions with the surface. Therefore, sophisticated radiative transfer models have been developed to calculate the radiance field. The transfer models are based on the *Radiative Transfer Equation* (see chapter 4).

Using such a radiative transfer model, we can develop a *Forward Model*, which maps atmospheric parameters to a measured signal. To be precise, consider some state vector $\boldsymbol{x}$ containing atmospheric parameters. Then, the forward model $\boldsymbol{F}$ maps the state to a measured radiance $\boldsymbol{y}$. To retrieve atmospheric properties from the measurement, the forward model has to be inverted.

2.2 Aerosol Layer Height Algorithm

The Aerosol Layer Height algorithm is an algorithm developed at KNMI. Its main goal is the retrieval of aerosol height information from radiance spectra measured by TROPOMI. See [6] and [7] for a detailed description of this algorithm. It has the following key features:

- A forward model with full multiple scattering radiative transfer computations in the O_2 A band using the DISAMAR software package. Computations are made for an atmospheric model describing an atmosphere with scattering and absorption by molecules and aerosols, and which is bounded by a reflecting Lambertian surface.

- Regularized inversion of the forward model through means of Optimal Estimation, which exploits prior knowledge of the physical quantities involved.
- A simple aerosol profile parameterization, where we assume that the aerosol is homogeneously contained in a single layer with a fixed pressure thickness.
- Retrieval of the following main fit parameters: aerosol layer height (mid pressure), the aerosol layer's optical thickness, and the surface albedo (wavelength dependent).

In the following, we will briefly elaborate on these key features.

2.2.1 DISAMAR

The Determining Instrument Specifications and Analyzing Methods for Atmospheric Retrieval program (DISAMAR), is a computer program developed at KNMI. See [14] for a detailed description of the program. DISAMAR is the science code, which functions as the basis for the operational TROPOMI Aerosol Layer Height algorithm. The version of DISAMAR we use is V3.5.3.

DISAMAR can be used for radiative transfer simulations to compute spectra. Radiative transfer simulations are performed with the approximation method called Layer Based Orders of Scattering (LABOS), which is an efficient variant of the adding/doubling method (see [15]). The LABOS approximation method accounts for multiple scattering by molecules and aerosol, absorption by aerosol, absorption by oxygen, and also accounts for a reflecting surface. Instrument properties, like spectral resolution, are also accounted for.

In DISAMAR we distinguish two simulation modes appropriate to our application:

- The first mode simulates spectra for a simplified aerosol model. This simplified model is the same as used in the Aerosol Layer Height algorithm. We call it the forward model for retrieval. Spectra that are computed from this model can be compared to (a simulation of) real measured spectra. By changing the parameters of the aerosol model, we can fit the spectra, and therefore also the parameters. With this mode we can simulate retrievals of the Aerosol Layer Height algorithm if we fit the parameters according to the same inversion method as the Aerosol Layer Height algorithm.
- The second mode's primary function is the simulation of radiance measurements. By carefully specifying the composition of the atmosphere, we can approximate

a realistic atmosphere. For example, large amounts of homogeneously distributed aerosol layers can be used to approximate an aerosol profile. We can use this mode to obtain measured radiance spectra without actually doing any real measurements. We call this the forward model for simulation.

These simulation modes are valuable for exploratory research of the Aerosol Layer Height algorithm, since it is very important to have a thoroughly tested algorithm before launch.

2.2.2 Optimal Estimation

The inversion of the forward model is typically an underdetermined problem. We can constrain the problem using a priori information of the state atmospheric state. For example, we know that aerosols are usually only found between 0 and 8 km and not in the rest of the atmosphere. The regularization method we use is called optimal estimation, and is based on Bayes' Theorem. Here, we briefly describe the basic idea of optimal estimation.

Suppose that we have prior information (before doing a measurement) on the distributions of the measurements and the state. Denoting $\mathbb{P}(\boldsymbol{Y}|\boldsymbol{X})$ and $\mathbb{P}(\boldsymbol{X})$ for the prior measurement and prior state distributions, and writing $\mathbb{P}(\boldsymbol{X}|\boldsymbol{Y})$ for the posterior (after the measurement) distribution of the state, then Bayes' Theorem states that

$$\mathbb{P}(\boldsymbol{X}|\boldsymbol{Y}) \propto \mathbb{P}(\boldsymbol{Y}|\boldsymbol{X})\mathbb{P}(\boldsymbol{X}). \tag{2.1}$$

The forward model $\boldsymbol{F}$ maps an atmospheric state $\boldsymbol{x}$ to a radiance measurement $\boldsymbol{y}$. That is,

$$\boldsymbol{y} = \boldsymbol{F}(\boldsymbol{x};\boldsymbol{b}) + \boldsymbol{\epsilon}, \tag{2.2}$$

where $\boldsymbol{b}$ are model parameters and $\boldsymbol{\epsilon}$ are random measurement errors.

Furthermore, assume that the measurement errors are Gaussian with zero mean and covariance $\boldsymbol{\Sigma}_{\boldsymbol{\epsilon}}$, then $\mathbb{P}(\boldsymbol{y}|\boldsymbol{x})$ is also Gaussian:

$$\mathbb{P}(\boldsymbol{y}|\boldsymbol{x}) = \frac{1}{(2\pi)^{m/2}|\boldsymbol{\Sigma}_{\epsilon}|^{1/2}}\exp\left(-\frac{1}{2}(\boldsymbol{y}-\boldsymbol{F}(\boldsymbol{x}))^T\boldsymbol{\Sigma}_{\boldsymbol{\epsilon}}^{-1}(\boldsymbol{y}-\boldsymbol{F}(\boldsymbol{x}))\right). \tag{2.3}$$

Next, assume that the prior state is also Gaussian distributed, with mean $\boldsymbol{x}_a$ and covariance matrix $\boldsymbol{\Sigma}_a$, i.e.

$$\mathbb{P}(\boldsymbol{X}) = \frac{1}{(2\pi)^{n/2}|\boldsymbol{\Sigma}_a|^{1/2}}\exp\left(-\frac{1}{2}(\boldsymbol{x}-\boldsymbol{x}_a)^T\boldsymbol{\Sigma}_{\boldsymbol{a}}^{-1}(\boldsymbol{x}-\boldsymbol{x}_a)\right). \tag{2.4}$$

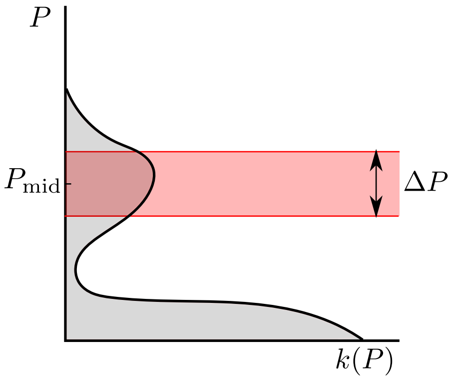

FIGURE 2.2: Schematic drawing of a realistic aerosol extinction profile (gray) and the parameterization used in the Aerosol Layer Height algorithm (red). Here, P is the pressure, $k(P)$ is the aerosol extinction at pressure P, ΔP is the pressure thickness of the aerosol layer, and P_{mid} is the mid pressure of the aerosol layer.

Then, the posterior distribution, $\mathbb{P}(\boldsymbol{x}|\boldsymbol{y})$, is also Gaussian distributed:

$$\mathbb{P}(\boldsymbol{x}|\boldsymbol{y}) \propto \exp\left(-\frac{1}{2}\left[(\boldsymbol{y}-\boldsymbol{F}(\boldsymbol{x}))^T \boldsymbol{\Sigma}_{\boldsymbol{\epsilon}}^{-1}(\boldsymbol{y}-\boldsymbol{F}(\boldsymbol{x})) + (\boldsymbol{x}-\boldsymbol{x}_a)^T \boldsymbol{\Sigma}_{\boldsymbol{a}}^{-1}(\boldsymbol{x}-\boldsymbol{x}_a)\right]\right). \quad (2.5)$$

Now, since we know the distribution for the posterior state, we can find the value of the posterior state that is most likely, given the measurement. The *Maximum A Posteriori Probability* estimate $\hat{\boldsymbol{x}}$ for the state $\boldsymbol{x}$, which we will call the *retrieval solution* is given by

$$\hat{\boldsymbol{x}} = \arg\min \chi^2, \quad (2.6)$$

where

$$\chi^2 = \underbrace{(\boldsymbol{y}-\boldsymbol{F}(\boldsymbol{x}))^T \boldsymbol{\Sigma}_{\boldsymbol{\epsilon}}^{-1}(\boldsymbol{y}-\boldsymbol{F}(\boldsymbol{x}))}_{\text{weighted least-squares}} + \underbrace{(\boldsymbol{x}-\boldsymbol{x}_a)^T \boldsymbol{\Sigma}_{\boldsymbol{a}}^{-1}(\boldsymbol{x}-\boldsymbol{x}_a)}_{\text{prior state deviation penalization}}. \quad (2.7)$$

Basically, this is a weighted least-squares fit for the measurement, with an additional penalization term for deviations from the prior state.

Due to the non-linearity of the forward model, we employ a Newton iteration scheme to minimize χ^2. This Newton iteration scheme is described in [16].

2.2.3 Parameterization of the Aerosol Vertical Profile

Aerosols have a certain vertical distribution, which is often characterized by an extinction profile, i.e. the amount of extinction (scattering plus absorption) due to aerosols at some altitude or pressure level at a particular wavelength (often 550 nm). Based on the experiences with cloud height retrievals, a different parameterization of the aerosol profile is assumed in the retrieval of aerosol height.

We assume that the aerosol profile consists of one layer of a fixed pressure thickness ΔP with homogeneously distributed aerosol. This aerosol layer's mid pressure is located at the pressure P_{mid}. See Figure 2.2 for a schematic overview of the parameterization versus a realistic aerosol profile. For this parameterized aerosol profile, we fit the layer's mid pressure and its optical thickness (a measure for the amount of aerosol). Furthermore, we also fit the reflectivity of the surface.

Of course, the simplified parameterization of the aerosol profile is a modeling error and has important consequences. What these consequences are and how we should interpret the retrieved parameters, will be the topic of this research.

Chapter 3

Retrieval Simulations

3.1 Introduction

In this chapter, we perform Aerosol Layer Height retrieval simulations for spectra simulated for atmospheres with realistic aerosol profiles. We do this to investigate the behavior of the Aerosol Layer Height algorithm in realistic situations. First, we collect aerosol profile data that is representative of profiles that we expect to observe in nature. Then, we perform the actual retrieval experiment.

3.2 Aerosol Profiles

The Cloud-Aerosol Lidar with Orthogonal Polarization (CALIOP) Lidar, aboard the CALIPSO satellite, has been acquiring aerosol extinction profiles from all over the world for six years now. This data has been aggregated into a climatology, in which monthly mean profiles of aerosol extinction coefficients (at 532 nm) are reported on a $2^\circ \times 5^\circ$ lat-long global grid, see [5].

From this climatology, we select eight different regions for which we derive generic aerosol profiles. Four regions are located at sea and four are continental regions. Of course, there is a seasonal dependence, so we also need to distinguish a time period of interest. We pick the months of highest aerosol load. The regions are as follows:

- Central Atlantic (CAT), to the west of North Africa. Desert dust from the Sahara is advected over the ocean. This often leads to elevated aerosol. This aerosol is observed year-round, with peak loads in July.

- South Atlantic (SAT), to the west of South Africa. Aerosol from biomass burning (forest fires) is advected from the continent to the ocean. In this region, most aerosol is observed in September.
- North West Pacific (NWP), to the east of China. Aerosol from industrial pollution is advected eastward from China to the ocean. Most aerosol is observed during springtime, so we pick April as the month of interest.
- South Pacific (SPA). In this remote region we only observe sea salt aerosol. This region does not have any months of extraordinary aerosol production, so we arbitrarily pick July.
- Central Europe (CEU). In this region we observe industrial pollution, but only a little relative to, say, the industrial parts of China. The aerosol loading in Europe is very small year-round, so we again pick July arbitrarily.
- North African desert (NAD), the Sahara. The desert dust that is observed over this region has highest loads in July.
- South African land (SAL). Forest fires leading to biomass burning aerosols are most frequent in July. Obviously, we also observe the highest load then.
- East China industry (ECI). High loads of industrial pollution are observed in this industrial part of China year-round. However, there is a small peak in production during spring, so we pick April as our month of interest for the China region.

Figure 3.1 displays these regions on a map, and Table 3.1 shows a more detailed description of the exact latitudes and longitudes of the regions and their month of interest.

We also attribute an appropriate aerosol model to each region. Such an aerosol model defines the optical properties of the aerosol, which typically vary for different types of aerosol. For example, sea salt and ash from biomass burning exhibit significantly different interactions with light, since sea salt only scatters light, while ash from biomass burning also absorbs. We choose between four aerosol models, i.e. desert dust (DD), sea salt (SS), strongly absorbing (SA) and weakly absorbing (WA). The details of the aerosol models are discussed in section 5.5. The regions where desert dust is found, CAT and NAD, use the DD model. The SPA region uses the SS model. We use the WA aerosol model for the regions exhibiting industrial pollution, i.e. ECI, NWP and CEU. The biomass burning regions, SAT and SAL use the SA model.

For every region, we collect the CALIOP extinction profiles for the month of interest in the year 2012, and take the average over these profiles to obtain a mean profile, see

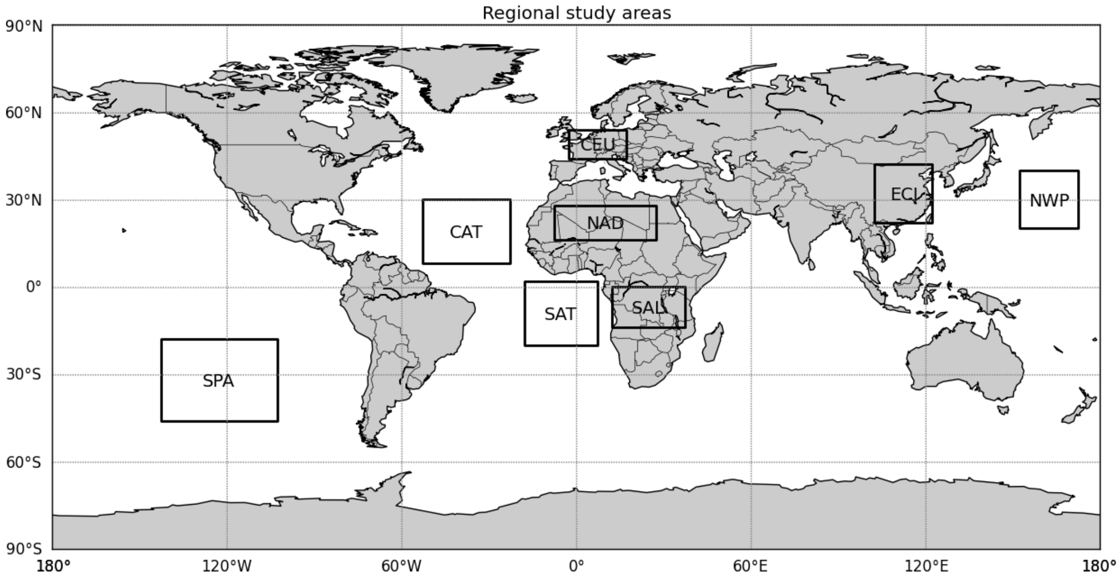

FIGURE 3.1: Global map displaying the regions used to select aerosol extinction profiles from the CALIOP data.

Scene	Latitudes	Longitudes	Month	Aer. Mdl.
CAT	$8°N$–$30°N$	$52.5°W$– $22.5°W$	July	DD
SAT	$20°S$ – $2°N$	$17.5°W$– $7.5°E$	Sept	SA
NWP	$20°N$–$40°N$	$152.5°E$ –$172.5°E$	April	WA
SPA	$46°S$ –$18°S$	$142.5°W$–$102.5°W$	July	SS
CEU	$44°N$–$54°N$	$2.5°W$– $17.5°E$	July	WA
NAD	$16°N$–$28°N$	$7.5°W$– $27.5°E$	July	DD
SAL	$14°S$ – $0°$	$12.5°E$ – $37.5°E$	Sept	SA
ECI	$22°N$–$42°N$	$102.5°E$ –$122.5°E$	April	WA

TABLE 3.1: Data defining the selection regions for the CALIOP data. For an explanation of the abbreviations, see the text.

Figure 3.2. Each of the eight average profiles is used as the typical profile for each region in our simulations.

For implementation of our aerosol profiles in DISAMAR, we need to discretize the profiles. Since we can only define layers with homogeneously distributed aerosol, we cover the extinction profile with layers of constant extinction, see Figure 3.3.

3.3 Aerosol Layer Height Retrieval Simulations for Realistic Aerosol Profiles

We simulate measured spectra with DISAMAR using the discretizations of our extinction profiles, as discussed in the previous section. Then, we perform Aerosol Layer Height retrievals on these simulated spectra assuming a single elevated layer in the retrieval.

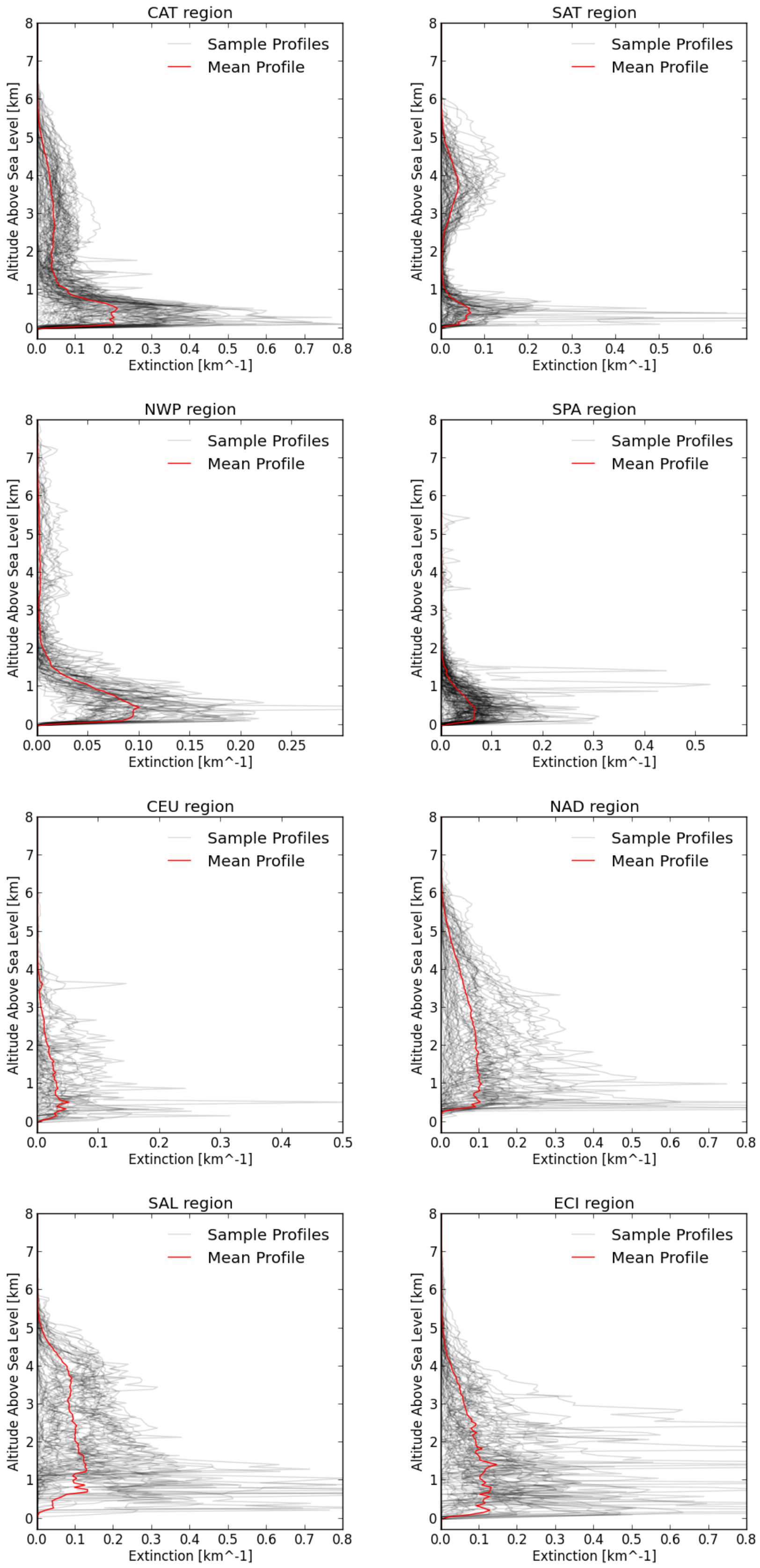

Figure 3.2: Mean aerosol extinction profiles for all typical aerosol scenes (red), and the CALIOP extinction profiles from which the mean profiles are calculated (transparent black).

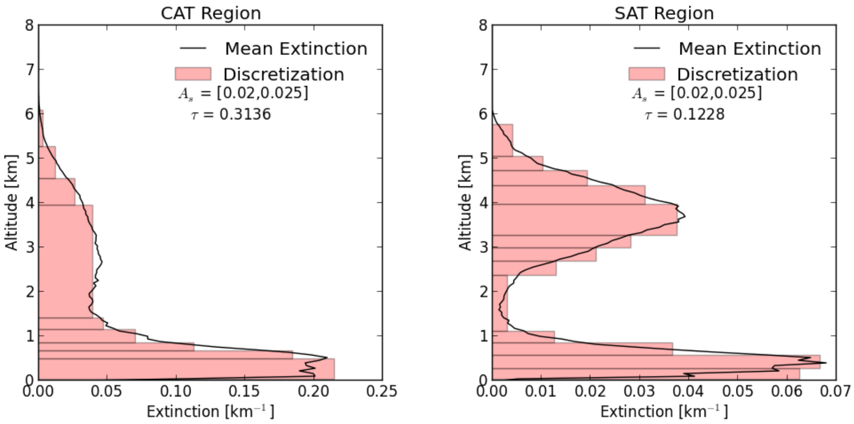

FIGURE 3.3: Mean-Extinction profiles (black) for the CAT (left) and SAT (right) scenes and their corresponding discretizations for DISAMAR (red). The wavelength nodes for the surface albedo, A_s, are at 758 and 770 nm. The optical thickness of the aerosol profile is denoted by τ.

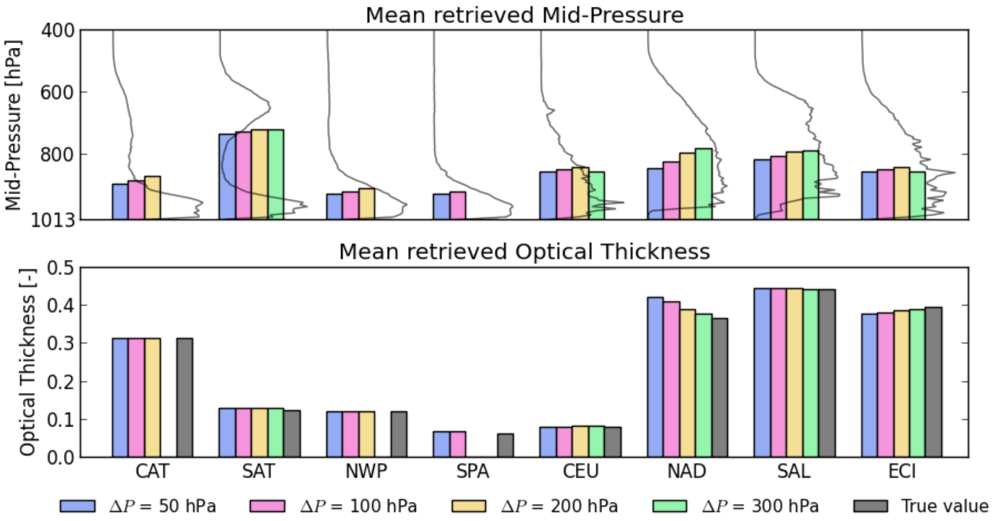

FIGURE 3.4: Retrieval results when not fitting the surface albedo for all scenes. Top: Mean retrieved mid pressure. Bottom: Mean retrieved optical thickness. The colors represent the results for different pressure thicknesses, ΔP. For easy comparison, the true extinction profiles, and true optical thicknesses are shown in gray. Missing bars indicate that the retrievals did not converge.

In this initial investigation, we do not fit the surface albedo, as opposed to the default Aerosol Layer Height algorithm setup. Thus, the fit parameters are the aerosol layer optical thickness and the aerosol layer mid pressure.

We vary the a priori mid pressure from 400 to about 900 hPa to investigate whether we obtain a global minimum. If we have multiple minima, the solution probably depends on the starting value of the aerosol layer's mid pressure. The step size of the prior mid pressures is 10 hPa. The a priori optical thickness is given by the total optical thickness of the aerosol profile. Furthermore, we do the same experiment for four different values of the pressure thickness of the aerosol layer, i.e. $\Delta P = 50$, 100, 200, and 300. All other model parameters (e.g. the aerosol microphysical properties) are assumed to be known. The a priori standard deviation for the optical thickness is given by 1, and for the mid pressure it is given by 500 hPa, effectively giving both parameters the freedom to move throughout the entire parameter space. The maximum number of Newton iterations we allow is 12.

As the retrieval results are very stable, we show the mean retrieval results in Figure 3.4. The following observations can be made:

- The retrievals show good convergence. Only in three settings we see no convergence. The settings that do show convergence have a 100% convergence ratio.
- For the cases where we do not have convergence, we observe that the algorithm stopped because the aerosol layer was repeatedly placed partly below the surface. This happened with a 200 hPa layer for the SPA scene and with a 300 hPa layer for both the CAT and SPA scene. Indeed, these scenes have aerosols close to the surface.
- Very stable retrieved parameters are found. When looking at each scene's largest deviation from the mean, the largest of these deviations is smaller than 1 hPa for the mid-pressure and less than $5 \cdot 10^{-4}$ for the optical thickness.
- A small variation in retrieved parameter values is found for different pressure thicknesses. For the NAD scene we see variations of about 80 hPa, and 0.05 in the optical thickness. The variations in the other scenes are much smaller.
- The retrieved optical thickness tends to be equal or very close to the true optical thickness of the aerosol extinction profile.
- The retrieved mid-pressures all lie somewhere inside the aerosol profile. It seems reasonable that this height is some centroid of the aerosol extinction profile.

Summarizing, we generally find very stable results with good convergence. The optical thickness we retrieve tends to match the true optical thickness of the aerosol extinction profile. Furthermore, the retrieved Aerosol Layer Height can probably be interpreted as some kind of centroid of the aerosol extinction profile. We treat this interpretation in more detail in chapter 7. Before we can do this, however, we first need to develop a thorough understanding of the radiative transfer, and its modeling, which is the subject of the following chapters.

Chapter 4

Radiative Transfer Equation

4.1 General Radiative Transfer Equation

The forward model needed in retrieval calculates the TOA radiance for a model atmosphere. Basically, it does so by solving the radiative transfer equation. Here, we introduce the radiative transfer equation.

Consider a beam of radiation traversing some medium. The beam of radiation will be weakened (extinguished) by its interaction with matter inside the medium: photons get absorbed or scattered out of the beam. Additionally, radiation may also be strengthened by scattering of photons into the beam.

Denote $I_\lambda(s)$ for the intensity of the radiation of wavelength λ at a distance s along the beam. This quantity is measured in photons/m^2/nm/s/sr. The intensity after traversing a slab of the medium with thickness $\mathrm{d}s$ in the direction of propagation becomes $I_\lambda(s + \mathrm{d}s) = I(s) + \mathrm{d}I_\lambda(s)$. See Figure 4.1.

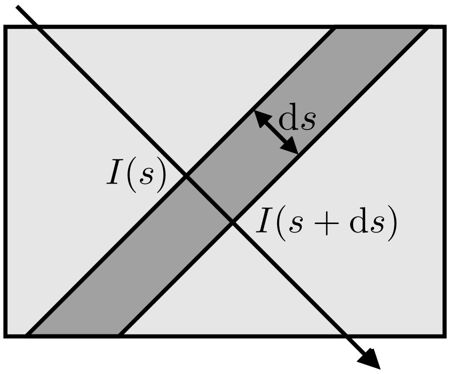

FIGURE 4.1: Schematic drawing of a beam of radiation propagating through a medium (light gray), containing a slab of thickness $\mathrm{d}s$ (dark gray).

The Lambert-Beer law (e.g. [17] or [18]) states that, the loss in radiation is proportional to the thickness of the slab, and the initial intensity, i.e.

$$\mathrm{d}I_\lambda(s) = -k_\lambda^{\mathrm{ext}}(s) I_\lambda(s) \mathrm{d}s, \tag{4.1}$$

where the *extinction coefficient* $k_\lambda^{\mathrm{ext}}(s)$ is a proportionality constant, which is measured in inverse unit length.

Now, define the *extinction cross section* $\sigma_\lambda^{\mathrm{ext}}$ such that

$$k_\lambda^{\mathrm{ext}}(s) = \sigma_\lambda^{\mathrm{ext}}(s) n(s), \tag{4.2}$$

where $n(s)$ is the number density of the particles responsible for extinction, measured in molecules per unit volume. Thus, the extinction cross section, measured in unit area per molecule, can be interpreted as an effective area of extinction for a single molecule.

The extinction cross section can be written as the sum of the *absorption cross section* $\sigma_\lambda^{\mathrm{abs}}$ and the *scattering cross section* $\sigma_\lambda^{\mathrm{sca}}$, i.e.

$$\sigma_\lambda^{\mathrm{ext}} = \sigma_\lambda^{\mathrm{abs}} + \sigma_\lambda^{\mathrm{sca}}. \tag{4.3}$$

This decomposition in absorption and scattering also leads to the definition of the *absorption coefficient* $k_\lambda^{\mathrm{abs}} = \sigma_\lambda^{\mathrm{abs}}(s) n(s)$ and the *scattering coefficient* $k_\lambda^{\mathrm{sca}} = \sigma_\lambda^{\mathrm{sca}}(s) n(s)$.

We define the positive contribution to the beam of radiation as

$$\mathrm{d}I_\lambda = j_\lambda(s) n(s) \mathrm{d}s, \tag{4.4}$$

where $j_\lambda(s)$ is the *source function coefficient.*

The negative and positive effects, (4.1) and (4.4), can be combined to obtain the *radiative transfer equation*

$$\frac{\mathrm{d}I_\lambda}{k_\lambda^{\mathrm{ext}} \mathrm{d}s} = -I_\lambda + J_\lambda, \tag{4.5}$$

where $J_\lambda = j_\lambda / \sigma_\lambda^{ext}$ is the *source function.*

4.2 Plane-Parallel Coordinates

In the previous, we worked with coordinates along some arbitrary path. Here, we define appropriate atmospheric coordinates.

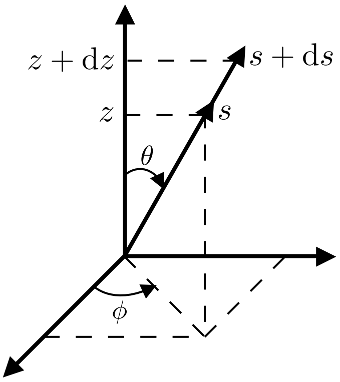

FIGURE 4.2: Graphic displaying the geometry of the plane-parallel coordinate system. The altitude relative to the surface is given by z. The azimuthal angle is given by ϕ. The zenith angle is given by θ. The distance along a beam of radiation is given by the (path) coordinate s.

We assume that we have a planar atmosphere, which consists of stacked horizontally homogeneous slabs. Writing z for the distance normal to the surface, θ for the inclination to the upward normal, and ϕ for the (counter-clockwise) azimuthal angle, we obtain so-called *Plane-Parallel Coordinates*. The geometry is shown in Figure 4.2.

Using plane-parallel coordinates, we rewrite the radiative transfer equation (4.5) as

$$\cos\theta \frac{\mathrm{d}I(z,\theta,\phi)}{k^{\text{ext}}(z)\mathrm{d}z} = -I(z,\theta,\phi) + J(z,\theta,\phi), \tag{4.6}$$

since $\mathrm{d}s = \frac{1}{\cos\theta}\mathrm{d}z$.

Next, we define the height variable *optical depth* $\tau(z)$ as

$$\tau(z) = \int_z^\infty k^{\text{ext}}(z')\mathrm{d}z'. \tag{4.7}$$

Then, $\mathrm{d}\tau = -k^{\text{ext}}(z)\mathrm{d}z$, and (4.6) simplifies to

$$u\frac{\mathrm{d}I(\tau,u,\phi)}{\mathrm{d}\tau} = I(\tau,u,\phi) - J(\tau,u,\phi), \tag{4.8}$$

where $u = \cos\theta$ is the *direction cosine.*

The *optical thickness* of the atmosphere, τ^*, is defined as

$$\tau^* = \int_0^\infty k^{\text{ext}}(z')dz', \tag{4.9}$$

such that $\tau = \tau^*$ corresponds to the surface, and $\tau = 0$ corresponds to the top of the atmosphere.

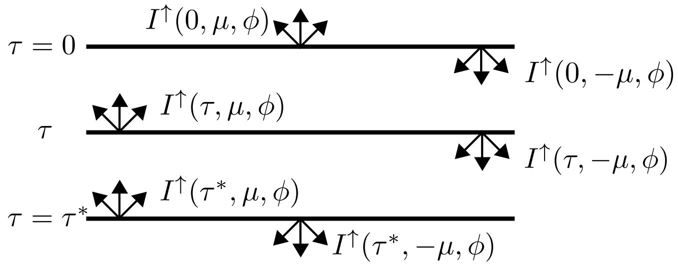

FIGURE 4.3: Schematic drawing of the half-range-quantities. The upward and downward radiance are given by $I^{\uparrow}$ and $I^{\downarrow}$, respectively. The atmosphere is bounded by the top of the atmosphere $\tau = 0$ and the surface $\tau = \tau^*$.

We can distinguish the two cases $u > 0$ and $u < 0$ in the radiative transfer equation (4.8). The case where $u > 0$ corresponds to upward radiation, and $u < 0$ corresponds to downward radiation. A useful convention is to define $\mu = |u|$, such that $I^{\uparrow}(\mu)$ and $I^{\downarrow}(-\mu)$ correspond to the upward and downward radiance, respectively (we include the arrows for easier reading). Figure 4.3 gives a schematic overview of these so-called *half-range quantities.*

4.3 General Solution

In this section, we derive the general form of the solution to the radiative transfer equation for plane-parallel atmospheres, (4.8). We do this by using the concept of integrating factors.

Consider the radiative transfer equation (4.8) for the upward intensity $I^{\uparrow}(\mu)$. Multiplying both sides with the integrating factor $e^{-\tau/\mu}$, and rewriting the equation yields

$$\left[\frac{\mathrm{d}I^{\uparrow}(\tau, \mu, \phi)}{\mathrm{d}\tau} - \frac{1}{\mu} I^{\uparrow}(\tau, \mu, \phi)\right] e^{-\tau/\mu} = -\frac{1}{\mu} J(\tau, \mu, \phi). \tag{4.10}$$

We recognize a derivative on the left hand side

$$\left[\frac{\mathrm{d}I^{\uparrow}(\tau, \mu, \phi)}{\mathrm{d}\tau} - \frac{1}{\mu} I^{\uparrow}(\tau, \mu, \phi)\right] e^{-\tau/\mu} = \frac{\mathrm{d}}{\mathrm{d}\tau} I^{\uparrow}(\tau, \mu, \phi) e^{-\tau/\mu}, \tag{4.11}$$

such that

$$\frac{\mathrm{d}}{\mathrm{d}\tau} I^{\uparrow}(\tau, \mu, \phi) e^{-\tau/\mu} = -\frac{1}{\mu} J(\tau, \mu, \phi). \tag{4.12}$$

Integrating both sides over $\tau' \in [\tau, \tau^*]$ yields

$$\int_{\tau}^{\tau^*} \frac{\mathrm{d}}{\mathrm{d}\tau'} I^{\uparrow}(\tau', \mu, \phi) e^{-\tau'/\mu} \mathrm{d}\tau' = -\frac{1}{\mu} \int_{\tau}^{\tau^*} J(\tau', \mu, \phi) \mathrm{d}\tau'. \tag{4.13}$$

Using the Fundamental Theorem of Calculus we can now rewrite this as

$$I^{\uparrow}(\tau,\mu,\phi) = I^{\uparrow}(\tau^*,\mu,\phi)e^{-(\tau^*-\tau)/\mu} + \frac{1}{\mu}\int_{\tau}^{\tau^*} J(\tau',\mu,\phi)e^{-(\tau'-\tau)/\mu}\mathrm{d}\tau'. \tag{4.14}$$

Similarly, we can solve for the downward intensity $I^{\downarrow}(-\mu)$ to obtain

$$I^{\downarrow}(\tau,-\mu,\phi) = I^{\downarrow}(0,-\mu,\phi)e^{-\tau/\mu} + \frac{1}{\mu}\int_{0}^{\tau} J(\tau',-\mu,\phi)e^{-(\tau-\tau')/\mu}\mathrm{d}\tau'. \tag{4.15}$$

We see that in order to find the solution, we need to integrate over the source function J and apply boundary conditions. We specify both the source function and the boundary conditions in the following two sections.

4.4 The Source Function

The source function describes how a beam of radiation gets strengthened through scattering of photons into the beam. In general, it also describes a positive contribution through thermal emission, but we neglect thermal emission, since this contribution is negligible in the near-infrared wavelength range.

Radiation at a certain optical depth τ can be scattered into the direction (u,ϕ) through scattering from any incoming direction (u',ϕ'), where $u' \in [-1,1]$ and $\phi \in [0,2\pi]$. The scattering distribution describing the probability of scattering from (u',ϕ') to (u,ϕ) is defined by the *Phase Function* $P(\tau,u,\phi,u',\phi')$.

Define the *Single Scattering Albedo*, $\omega(\tau)$, as the fraction of available photons that are involved in a scattering process, i.e.

$$\omega(\tau) = \frac{k^{\mathrm{sca}}(\tau)}{k^{\mathrm{ext}}(\tau)}, \tag{4.16}$$

then we write the source function J as (see [17])

$$J(\tau,u,\phi) = \frac{\omega(\tau)}{4\pi}\int_{0}^{2\pi}\int_{-1}^{1} I(\tau,u',\phi')P(\tau,u,\phi,u',\phi')\mathrm{d}u'\mathrm{d}\phi', \tag{4.17}$$

where the factor $\frac{1}{4\pi}$ is a normalization constant of the phase function.

4.5 Boundary Conditions

We next specify boundary conditions for the radiative transfer equation. First, we define the boundary condition for the top of the atmosphere ($\tau = 0$) and second we define two possible boundary conditions for the surface ($\tau = \tau^*$).

We model the sunlight as collimated light, because the Sun is a light source which is extremely far away from the Earth. We can do so by posing the boundary condition

$$I^{\downarrow}(0, -\mu, \phi) = E_0 \delta(\mu - \mu_0)\delta(\phi - \phi_0), \tag{4.18}$$

where E_0 is the solar irradiance (measured in photons/m^2/nm/s), $(-\mu_0, \phi_0)$ are the angular properties of the sunlight, and δ is the Dirac delta distribution. The solar zenith angle $-\mu_0$ is strictly negative because sunlight always points downwards.

The upward radiance at the top of the atmosphere $I^{\uparrow}(0, \mu, \phi)$ is unconstrained, since this is what we want to calculate.

The first boundary condition for the surface we consider is that of a black surface. For a black, non-reflecting boundary, we set $I^{\uparrow}(\tau^*, \mu, \phi) = 0$ for all μ and ϕ. In this case, the radiative transfer equation greatly simplifies and we can often solve it analytically.

The second surface boundary condition is that of a surface that is reflecting. For our application, we assume a *Lambertian* surface, which means that the surface reflects the incoming light isotropically. Defining the *Surface Albedo*, A_s, as the fraction of upward to downward radiation at the surface, we obtain the boundary condition (see [17])

$$I^{\uparrow}(\tau^*) = \frac{A_s}{\pi} \int_0^{2\pi} \int_0^1 I^{\downarrow}(\tau^*, -\mu, \phi)\mu \mathrm{d}\mu \mathrm{d}\phi. \tag{4.19}$$

Unfortunately, this boundary condition depends on the unknown quantity $I^{\downarrow}(\tau^*, -\mu, \phi)$, which prevents us from easily solving the transfer equation.

4.6 Direct and Diffuse Component

We split the radiation field into two components; a *direct*, I_{dir}, and a *diffuse* component, I_{dif}, such that

$$I(\tau, u, \phi) = I_{\mathrm{dir}}(\tau, u, \phi) + I_{\mathrm{dif}}(\tau, u, \phi). \tag{4.20}$$

The direct component is that part of the incoming solar light that has not yet been scattered or absorbed, whereas the diffuse part has been scattered at least once. Light that has been reflected by the surface, and has not yet been scattered afterwards is also called direct, regardless of the amount of scattering before reflection. In the following, we specify the direct part, and derive a new transfer equation for the diffuse part.

The direct downward component of radiation is given by

$$I_{\mathrm{dir}}^{\downarrow}(\tau, -\mu, \phi) = E_0 e^{-\tau/\mu} \delta(\mu - \mu_0)\delta(\phi - \phi_0), \tag{4.21}$$

where the factor $e^{-\tau/\mu_0}$ accounts for the extinction of the boundary condition (4.18) along the direction of the sunlight.

For the direct upward component, we distinguish two cases. First, when the surface is black, there is no direct upward component, since any light going upward has to be scattered at least once. Thus,

$$I_{\mathrm{dir}}^{\uparrow}(\tau, \mu, \phi) = 0. \tag{4.22}$$

Second, for a reflecting surface, we have

$$I_{\mathrm{dir}}^{\uparrow}(\tau, \mu, \phi) = I^{\uparrow}(\tau^*) e^{-(\tau^* - \tau)/\mu}. \tag{4.23}$$

This is the light that is reflected by the surface according to the boundary condition (4.19), while accounting for the extinction along its path after reflection (now we have $\tau^* - \tau$ as optical depth because the light is traveling in the upward direction).

The radiative transfer equation for the direct and diffuse components separated is found by combining (4.8), (4.17) and (4.20):

$$\begin{aligned} u\frac{\mathrm{d}I_{\mathrm{dir}}}{\mathrm{d}\tau} + u\frac{\mathrm{d}I_{\mathrm{dif}}}{\mathrm{d}\tau} &= I_{\mathrm{dir}} + I_{\mathrm{dif}} \\ &- \frac{\omega(\tau)}{4\pi}\int_0^{2\pi}\int_0^1 I_{\mathrm{dir}}^{\uparrow}(\tau, \mu', \phi')P(\tau, u, \phi, \mu', \phi')\mathrm{d}\mu'\mathrm{d}\phi' \\ &- \frac{\omega(\tau)}{4\pi}\int_0^{2\pi}\int_0^1 I_{\mathrm{dir}}^{\downarrow}(\tau, -\mu', \phi')P(\tau, u, \phi, -\mu', \phi')\mathrm{d}\mu'\mathrm{d}\phi' \\ &- \frac{\omega(\tau)}{4\pi}\int_0^{2\pi}\int_0^1 I_{\mathrm{dif}}^{\uparrow}(\tau, \mu', \phi')P(\tau, u, \phi, \mu', \phi')\mathrm{d}\mu'\mathrm{d}\phi' \\ &- \frac{\omega(\tau)}{4\pi}\int_0^{2\pi}\int_0^1 I_{\mathrm{dif}}^{\downarrow}(\tau, -\mu', \phi')P(\tau, u, \phi, -\mu', \phi')\mathrm{d}\mu'\mathrm{d}\phi'. \end{aligned} \tag{4.24}$$

Now, since

$$u\frac{\mathrm{d}I_{\mathrm{dir}}}{\mathrm{d}\tau} = I_{\mathrm{dir}} \tag{4.25}$$

by definition, these terms cancel in (4.24).

Then, for the black surface case, substituting (4.21), (4.22) and (4.25) in (4.24) yields the radiative transfer equation for the diffuse radiation

$$u\frac{\mathrm{d}I(\tau,u,\phi)}{\mathrm{d}\tau}=I(\tau,u,\phi)-\frac{\omega(\tau)}{4\pi}\int_0^{2\pi}\!\!\int_{-1}^{1}I(\tau,u',\phi')P(\tau,u,\phi,u',\phi')\mathrm{d}u'\mathrm{d}\phi'-S_a(\tau,u,\phi),\tag{4.26}$$

where we have dropped the diffuse subscript, and S_a is the *single scattering source term*

$$S_a(\tau,u,\phi)=\frac{\omega(\tau)}{4\pi}E_0e^{-\tau/\mu_0}P(\tau,u,\phi,-\mu_0,\phi_0).\tag{4.27}$$

For the reflecting surface case, we substitute (4.21), (4.23) and (4.25) to obtain

$$\begin{aligned}u\frac{\mathrm{d}I(\tau,u,\phi)}{\mathrm{d}\tau}&=I(\tau,u,\phi)-S_a(\tau,u,\phi)-S_b(\tau,u,\phi)\\&\qquad-\frac{\omega(\tau)}{4\pi}\int_0^{2\pi}\!\!\int_{-1}^{1}I(\tau,u',\phi')P(\tau,u,\phi,u',\phi')\mathrm{d}u'\mathrm{d}\phi',\end{aligned}\tag{4.28}$$

where S_b is the *single scattering boundary source term*

$$S_b(\tau,u,\phi)=\frac{\omega}{4\pi}\int_0^{2\pi}\!\!\int_0^1P(u,\phi,\mu',\phi')e^{-(\tau^*-\tau)/\mu'}I^{\uparrow}(\tau^*)\mathrm{d}\mu'\mathrm{d}\phi',\tag{4.29}$$

and $I^{\uparrow}(\tau^*)$ satisfies the reflecting surface boundary condition (4.19), where $I^{\downarrow}(\tau^*,\mu',\phi')$ is indeed the total (both diffuse and direct) downward penetrating radiance.

Finally, we note that the equations for the diffuse radiation still have the same form as the radiative transfer equation for the total radiation (4.8). Hence, the method for finding the solution, as described in section 4.3, is still valid.

4.7 Multiple Atmospheric Constituents

When there are multiple atmospheric constituents that scatter, absorb or both, we need to adapt the radiative transfer equation.

Consider a set of atmospheric constituents, say Λ. For each atmospheric constituent, $i\in\Lambda$, we expect to see different cross sections, phase functions, and number densities, and thus we need to define $\sigma_i^{\mathrm{ext}}=\sigma_i^{\mathrm{abs}}+\sigma_i^{\mathrm{ext}}$, P_i, and n_i for each species $i\in\Lambda$.

Define the species specific extinction coefficient k_i^{ext} and similarly the species specific absorption and scattering coefficients as

$$k_i^{\mathrm{ext}}(z)=\sigma_i^{\mathrm{ext}}(z)n_i(z)=\sigma_i^{\mathrm{abs}}(z)n_i(z)+\sigma_i^{\mathrm{sca}}(z)n_i(z)=k_i^{\mathrm{abs}}(z)+k_i^{\mathrm{sca}}(z).\tag{4.30}$$

Then, the single scattering albedo of an atmospheric constituent i, $\omega_i(z)$, is defined as the fraction of available photons scattered by constituent i in the entire mixture:

$$\omega_i(z) = \frac{k_i^{\mathrm{sca}}(z)}{k^{\mathrm{ext}}(z)}, \tag{4.31}$$

where $k^{\mathrm{ext}}(z) = \sum_{i\in\Lambda} k_i^{\mathrm{ext}}(z)$. This definition may be somewhat unusual for a reader familiar with radiative transfer, but it is consistent with the following, and leads to elegant notation.

Finally, we incorporate the multiple atmospheric constituents in the radiative transfer equation in a straightforward manner as we write

$$u\frac{\mathrm{d}I(\tau,u,\phi)}{\mathrm{d}\tau} = I(\tau,u,\phi) - \sum_{i\in\Lambda} J_i(\tau,u,\phi), \tag{4.32}$$

where J_i, the species specific source function, is of course defined as

$$J_i(\tau,u,\phi) = S_{a,i}(\tau,u,\phi) + S_{b,i}(\tau,u,\phi) + \frac{\omega_i(\tau)}{4\pi}\int_0^{2\pi}\!\!\int_{-1}^{1} I(\tau,u',\phi')P_i(\tau,u,\phi,u',\phi')\mathrm{d}u'\mathrm{d}\phi', \tag{4.33}$$

with

$$S_{a,i}(\tau,u,\phi) = \frac{\omega_i(\tau)}{4\pi}E_0 e^{-\tau/\mu_0}P_i(\tau,\mu,\phi,-\mu_0,\phi_0), \tag{4.34}$$

and

$$S_{b,i}(\tau,u,\phi) = \frac{\omega_i(\tau)}{4\pi}\int_0^{2\pi}\!\!\int_0^{1} P_i(\tau,u,\phi,\mu',\phi')e^{-(\tau^*-\tau)/\mu'}I^{\uparrow}(\tau^*)\mathrm{d}\mu'\mathrm{d}\phi'. \tag{4.35}$$

In conclusion, to account for multiple atmospheric constituents involved with extinction, we only need to give each constituent its own separate source term, and account for species specific scattering behavior.

Chapter 5

Model Atmosphere and Instrument Model

5.1 Introduction

In chapter 4 we formulated the radiative transfer equation in a general form. Here, we specify quantities required to perform computations.

5.2 Solar Irradiance

A high-resolution solar spectrum E_0 is required for the calculation of the radiance field. We use the reference solar irradiance spectrum according to [19].

5.3 Surface Albedo

The surface albedo A_s typically depends on wavelength. In our fit window (758-770 nm), this wavelength dependence can be approximated by a linear dependence, see [20].

We specify the surface albedo at two wavelength nodes, 758 and 770 nm, and perform linear interpolation for any wavelength in between these nodes. For simulating a measurement above a sea surface, we use the values 0.02 and 0.025, respectively. Land exhibits a much stronger surface reflection. There, the values are given by 0.2 and 0.25 for vegetated land and 0.3 and 0.35 for desert regions. These values are based on the findings in [20].

5.4 Molecules

Molecular scattering is modeled by Rayleigh scattering, a term that gets its name from Lord Rayleigh, who first derived the wavelength dependence of this particular scattering process, see e.g. [21].

In the years after Rayleigh's initial research, Rayleigh scattering remained a popular subject of study and many improvements have been made to Rayleigh's original findings. One, somewhat modern, formula for the Rayleigh scattering cross section is given by (see [22], [23] and [24])

$$\sigma_{\text{mol}}^{\text{sca}} = \frac{24\pi^3}{\lambda^4 n_{\text{ref}}^2} \frac{(N^2-1)^2}{(N^2+2)^2} \frac{6+3\delta(\lambda)}{6-7\delta(\lambda)}, \tag{5.1}$$

where δ is the depolarization factor, n_{ref} is the number density of air molecules at some reference altitude and N is the refractive index of air.

The Rayleigh scattering phase function is given by

$$P_{\text{mol}}(\mu, \phi, \mu', \phi') = \frac{3(45+\epsilon)(1+\cos^2\Theta)+36\epsilon}{180+40\epsilon}, \tag{5.2}$$

where Θ is the *single scattering angle* (see [18], Appendix F, for a derivation)

$$\Theta = \cos^{-1}\left(\sin(\theta)\sin(\theta')\cos(\phi-\phi') - \cos(\theta)\cos(\theta')\right), \tag{5.3}$$

and

$$\epsilon(\lambda) = \frac{45\delta(\lambda)}{6-7\delta(\lambda)}. \tag{5.4}$$

Molecules can also absorb radiation. The strongest absorption process in the O_2 A band is line absorption by oxygen. The absorption cross section corresponding to this absorption process, $\sigma_{O_2}^{\text{abs}}$, is carefully studied, and can be obtained from online databases, like the Jet Propulsion Laboratory database[1]. This cross section exhibits strong spectral variations, see Figure 5.1 for the absorption optical thickness.

For computations based on the single scattering approximation discussed in chapter 6, we only consider Rayleigh scattering and absorption by oxygen. Only the line parameters from the most abundant isotopes are used, and are also taken from the Jet Propulsion Laboratory database. For simulations with DISAMAR, we accidentally also included first-order line mixing and collision-induced absorption by O_2-O_2 and O_2-N_2 according to [25] and [26]. We expect that this error does not have a significant effect on the results.

---

[1] `http://spec.jpl.nasa.gov/`

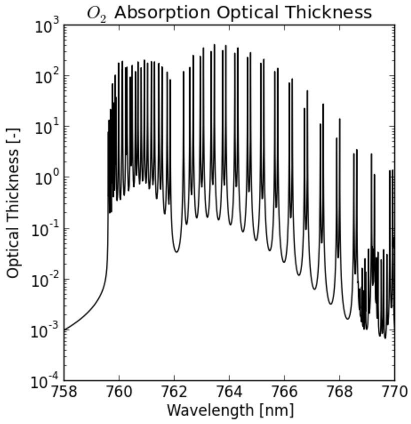

FIGURE 5.1: Absorption optical thickness of oxygen, as a function of wavelength, in the O_2 A band for some reference atmosphere. Note the logarithmic y-axis.

To fully specify scattering and absorption by molecules, the vertical distribution, or the height-dependent number densities, of the molecules are needed. We do this via a standard atmospheric model, the *Mid-Latitude Summer* atmospheric model, [27] Table 1b.

The standard atmospheric model determines an altitude, pressure and temperature grid, which we use to determine the density of air using the ideal gas law

$$\rho_{\text{air}}(z) = \frac{P(z)}{R_{\text{specific}} T(z)}, \tag{5.5}$$

where $\rho_{\text{air}}(z)$ is the mass density of air at altitude z, $P(z)$ is the pressure at altitude z, R_{specific} is the specific gas constant of air and $T(z)$ is the temperature at altitude z.

Once the mass density of air is known we determine its number density, $n_{\text{mol}}(z)$ as follows:

$$n_{\text{mol}}(z) = N_A \frac{\rho_{\text{air}}(z)}{m_{\text{air}}}, \tag{5.6}$$

where N_A is Avogadro's constant, and m_{air} is the molar mass of air.

Next, we assume that throughout the atmosphere the part of air that consist of oxygen is determined by a fixed mixing ratio (which is a valid assumption for all practical purposes, see [28] Table 1.2), and thus

$$n_{O_2}(z) = r_{\text{mix}} n_{\text{mol}}(z), \tag{5.7}$$

where r_{mix} is the mixing ratio of oxygen in air.

The exact values of the atmospheric constants and the mid-latitude summer profile are given in appendix C.

Model	$\sigma_{\text{aer}}^{\text{ext}}$ (μm^2)	$\sigma_{\text{aer}}^{\text{sca}}/\sigma_{\text{aer}}^{\text{ext}}$	g
WA	$1.079 \cdot 10^{-2}$	0.9703	0.5793
SA	$1.831 \cdot 10^{-2}$	0.7605	0.5669
SS	9.927	1	0.7547
DD	11.08	0.970	0.712

Table 5.1: Aerosol properties at the O_2 A band for the four standard aerosol models as proposed by the Aerosol-CCI project: Weakly Absorbing (WA), Strongly Absorbing (SA), Sea Salt (SS) and Desert Dust (DD). Reported aerosol properties are the extinction cross section, $\sigma_{\text{aer}}^{\text{ext}}$, the ratio $\sigma_{\text{aer}}^{\text{sca}}/\sigma_{\text{aer}}^{\text{ext}}$, and the assymetry parameter g.

5.5 Aerosol

The scattering and absorption properties of aerosol are determined by particle size, particle shape, and other optical properties like the bulk material's refractive index. These properties show strong spatial variations, as different processes play a role in the formation of aerosol all around the planet. These properties are carefully studied, see, for example, [29] and [30].

The Aerosol-CCI project, [31], proposes the use of four generic aerosol types to be used in modeling, which should be sufficient to cover natural variability in aerosol properties. These standard types are called *Weakly Absorbing* (WA), *Strongly Absorbing* (SA), *Sea Salt* (SS) and *Desert Dust* (DD). The Aerosol-CCI project reports all necessary properties to derive cross sections and phase functions. For (approximately) spherical particles, we can perform Mie calculations, [32], to achieve this and for particles that are non-spherical, we need to turn to other methods, like T-matrix calculations, [33].

The phase function for aerosol is often approximated by the *Henyey-Greenstein* phase function (HG phase function)

$$P_{\text{aer}}(\mu, \phi, \mu', \phi') = \frac{1 - g^2}{(1 + g^2 - 2g\cos\Theta)^{3/2}}, \tag{5.8}$$

where g is the *asymmetry parameter*. An easy calculation reveals that g is the first moment of the HG phase function and thus determines the expected direction of scattering. This phase function has no physical basis, but is an analytic fit to actual phase functions, which is very convenient for the use in computations. See Figure 5.2 for HG phase function approximations to the phase functions of the Aerosol-CCI generic models.

For our purposes, we use the cross sections and asymmetry parameters from the previously described Aerosol-CCI standard models, and approximate their phase functions with HG phase functions. These values are reported in table 5.1. Furthermore, we assume that these properties are wavelength independent. This is sufficient to fully

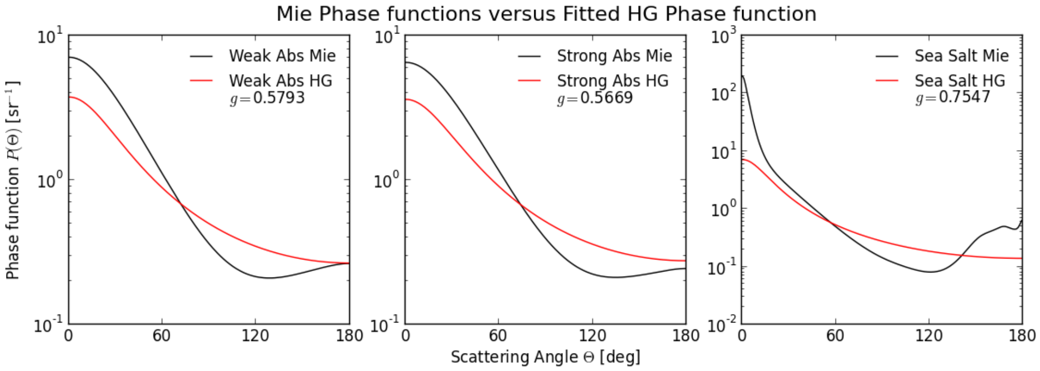

FIGURE 5.2: Mie Phase function (black) versus their fitted HG Phase functions (red) for the Aerosol-CCI aerosol models WA (left), SA (middle), and WA (right). All functions are given with the scattering angle Θ as independent variable. Note the logarithmic y-axes.

characterize the aerosol in our simulations for the different aerosol scenes discussed in section 3.2.

5.6 Instrument Response

Due to the measuring instrument's limitations, it is not possible to measure the radiation for each wavelength separately (monochromatic). Instead, the instrument observes the signal from small ranges of wavelengths binned together. We can model this limitation through means of the *Instrument Spectral Response Function* or the *Slit Function*.

When the high resolution radiance for some λ (and arbitrary μ and ϕ) is given by $I(\lambda)$ then the measured radiance $\hat{I}$ is obtained as

$$\hat{I}(\lambda) = D(\lambda)\int_{\lambda_{\text{min}}}^{\lambda_{\text{max}}} S(\lambda,\lambda')I(\lambda')d\lambda', \tag{5.9}$$

where $S(\lambda,\lambda')$ is the instrument spectral response function, D is some calibration constant and $\lambda_{\text{max}} = \lambda + 2\text{FWHM}$ and $\lambda_{\text{min}} = \lambda - 2\text{FWHM}$ define the convolution domain. Here, FWHM equals the *Full Width at Half Maximum*, i.e. the distance $\lambda - \lambda'$ required to have $S(\lambda,\lambda') = 0.5\max\{S\}$. Now, we model the IRF as a so-called flat-top function

$$S(\lambda,\lambda') = c2^{-2\left(\frac{\lambda-\lambda'}{w}\right)^4}, \tag{5.10}$$

where c is a normalization constant (we normalize such that $\int_{\lambda_{\text{min}}}^{\lambda_{\text{max}}} S(\lambda,\lambda')d\lambda' = 1$) and w defines the horizontal spread of the convolution window, and in our case is given by $w = 2^{-3/4}\text{FWHM}$, such that $S(\lambda,\lambda \pm \frac{1}{2}\text{FWHM}) = c/2$ (i.e. half the maximum).

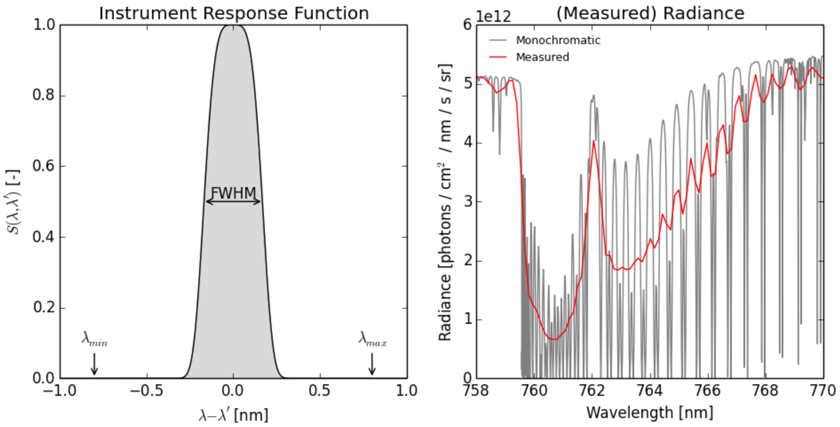

FIGURE 5.3: Left: The instrument response function $S(\lambda, \lambda')$ for the TROPOMI simulation settings. Right: The measured radiance after convolution with the slit function (red), plotted over the monochromatic radiance spectrum (gray) for some arbitrary atmosphere.

For TROPOMI, the full width at half maximum is estimated as FWHM $= 0.4$ (Private Communication). The instrument spectral response function belonging to this parameter, along with its effect on a spectrum, is shown in Figure 5.3.

Chapter 6

Single Scattering Approximation

6.1 Introduction

Here, we derive a single scattering approximation to the solution of the radiative transfer equation. This approximation only accounts for photons that are scattered once. Furthermore, we assume that the surface is black, i.e. non-reflecting. These approximations greatly simplify the source function, such that we can solve the radiative transfer equation analytically. We also derive semi-analytic derivatives for the top of atmosphere radiance.

6.2 Top of Atmosphere Radiance

Assume that the surface is black, i.e.

$$I^{\uparrow}(\tau^*) = 0, \tag{6.1}$$

and also assume that we only have single scattering, hence

$$J_i(\tau, u, \phi) = \frac{\omega_i(\tau)}{4\pi} E_0 P_i(u, \phi, -\mu_0, \phi_0) e^{-\tau/\mu_0}, \tag{6.2}$$

where the atmospheric constituents of interest are aerosol and molecules, i.e. $i \in \Lambda = \{\mathrm{aer}, \mathrm{mol}\}$.

Solving the radiative transfer equation (4.32) for the upward radiance yields

$$I^{\uparrow}(\tau, \mu, \phi) = I^{\uparrow}(\tau^*, \mu, \phi) e^{-(\tau^* - \tau)/\mu} + \frac{1}{\mu} \sum_{i \in \Lambda} \int_{\tau}^{\tau^*} J_i(\tau', \mu, \phi) e^{-(\tau' - \tau)/\mu} \mathrm{d}\tau', \tag{6.3}$$

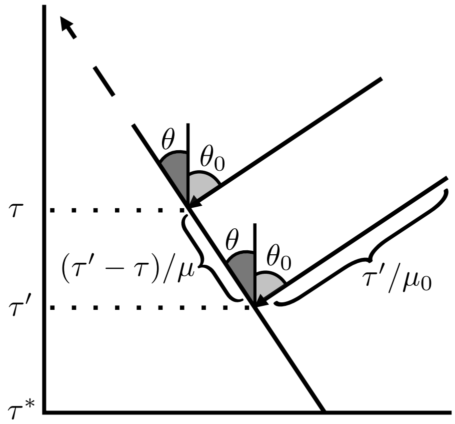

FIGURE 6.1: Schematic overview of how light paths contribute to the upward radiance $I^{\uparrow}(\tau, \mu, \phi)$. To obtain the total contribution, we need to integrate over all paths, for all optical depths τ' below τ, i.e. $\tau' \in [\tau, \tau^*]$.

which can be rewritten by substituting the expressions for the boundary condition (6.1) and the source (6.2):

$$I^{\uparrow}(\tau, \mu, \phi) = \frac{E_0}{4\pi\mu} e^{\tau/\mu} \sum_{i\in\Lambda} P_i(\mu, \phi, -\mu_0, \phi_0) \int_{\tau}^{\tau^*} \omega_i(\tau') e^{-\frac{\mu+\mu_0}{\mu\mu_0}\tau'} \mathrm{d}\tau'. \tag{6.4}$$

The previous result can also be explained more intuitively. We note that any radiance at (τ, μ, ϕ) is a contribution of photons that have been scattered a single time at some optical depth $\tau' > \tau$. Since we can explicitly write down the length of the individual light paths, i.e. $\tau'/\mu_0 + (\tau' - \tau)/\mu$ (see Figure 6.1), we can easily derive the attenuation along that path. Weighing each light path with its probability of occurring, and integrating over all optical depths $\tau' \in [\tau, \tau^*]$ yields the result.

To obtain the top of atmosphere radiance, $I^{\uparrow}_{\mathrm{TOA}}$, we simply substitute $\tau = 0$, which yields

$$I^{\uparrow}_{\mathrm{TOA}}(\mu, \phi) = \frac{E_0}{4\pi\mu} \sum_{i\in\Lambda} P_i(\mu, \phi, -\mu_0, \phi_0) \int_{0}^{\tau^*} \omega_i(\tau') e^{-\frac{\mu+\mu_0}{\mu\mu_0}\tau'} \mathrm{d}\tau'. \tag{6.5}$$

We remind that $\tau(z) = \int_z^{\infty} k^{\mathrm{ext}}(z')\mathrm{d}z'$, $\mathrm{d}\tau = -k^{\mathrm{ext}}(z)\mathrm{d}z$, and $\omega_i(z)k^{\mathrm{ext}}(z) = k_i^{\mathrm{sca}}(z)$. Then, the top of atmosphere radiance in terms of the altitude variable z is given by

$$I^{\uparrow}_{\mathrm{TOA}}(\mu, \phi) = \frac{E_0}{4\pi\mu} \sum_{i\in\Lambda} P_i(\mu, \phi, -\mu_0, \phi_0) \int_{0}^{\infty} k_i^{\mathrm{sca}}(z) e^{-\frac{\mu+\mu_0}{\mu\mu_0}\tau(z)} \mathrm{d}z. \tag{6.6}$$

We can evaluate the error of the single scattering approximation by comparing the top of atmosphere radiance of the approximation to the top of atmosphere radiance as simulated by DISAMAR. This comparison is shown in Figure 6.2 for the SPA and ECI

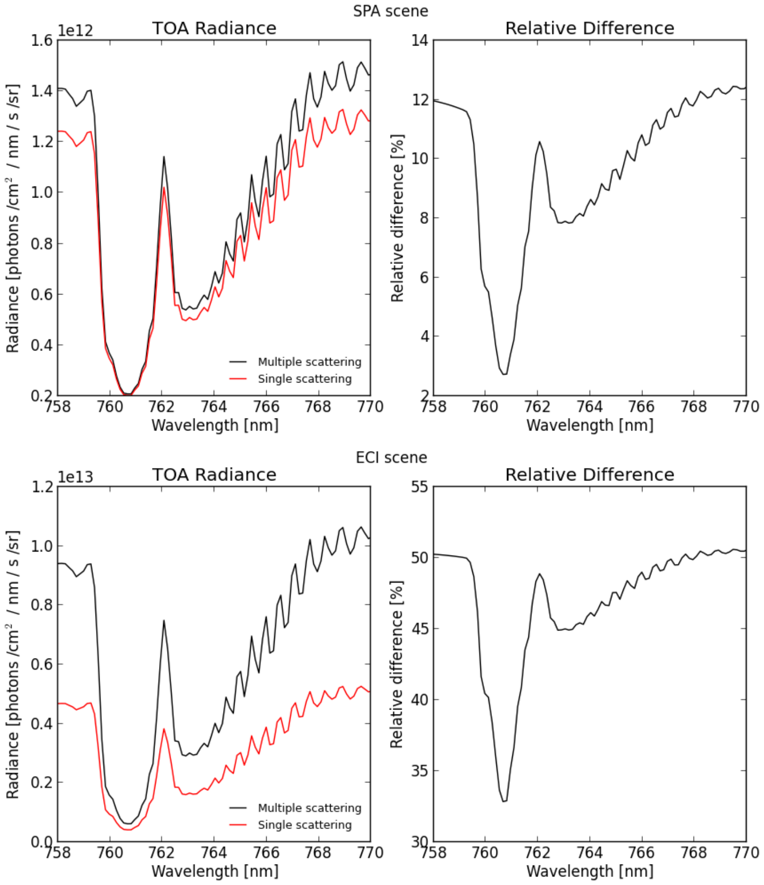

FIGURE 6.2: Top of atmosphere radiance for the single scattering approximation (red) and the full radiative transfer as computed by DISAMAR (black). The scenes shown are SPA (above) and ECI (below).

scenes. These two scenes were picked because they show the best and worst approximation, respectively.

We see that the single scattering approximation improves as we look inside the strong absorption regions (especially 760-762 nm). This is because photons with a longer path through the atmosphere are more likely to become absorbed. Thus, the measuring instrument is more likely to observe photons with a low order of scattering, since multiply scattered photons tend to have longer paths through the atmosphere than photons with low orders of scattering. Obviously, this effect is strongest in the strong absorption regions.

Another notable fact is that the approximation performs better for the scenes with a low aerosol optical thickness (not shown), because there is less chance of being scattered multiple times.

In conclusion, the single scattering approximation works best in a situation of high oxygen absorption and a low aerosol (scattering) optical thickness.

6.3 Monochromatic Derivatives

We investigate how strongly some arbitrary aerosol layer in the atmosphere contributes to the top of atmosphere radiance. We do this by perturbing the aerosol number density of some aerosol profile at a fixed height (z_0, z_1), and investigating the corresponding change in the top of atmosphere radiance, $I^{\uparrow}_{\text{TOA}}$. Taking the limit of the perturbation size of the number density to zero yields a semi-analytic derivative.

Consider the perturbed aerosol number density

$$\bar{n}_{\text{aer}}(z) = n_{\text{aer}}(z) + \eta 1\{z \in (z_0, z_1)\}. \tag{6.7}$$

Then, remembering the definition of the scattering/extinction coefficients $k^{\text{sca/ext}}_{\text{aer}}(z) = \sigma^{\text{sca/ext}}_{\text{aer}} n_{\text{aer}}(z)$, we also have perturbed aerosol scattering/extinction coefficients

$$\bar{k}^{\text{sca/ext}}_{\text{aer}}(z) = k(z) + \sigma^{\text{sca/ext}}_{\text{aer}} \eta 1\{z \in (z_0, z_1)\}, \tag{6.8}$$

while the scattering and extinction coefficients for the other constituents remain the same.

The total extinction coefficient, being the sum of the individual extinction coefficients, also changes. As a consequence, the optical depth also changes, i.e.

$$\bar{\tau}(z) = \int_z^\infty \bar{k}^{\text{ext}}(z')\mathrm{d}z' = \begin{cases} \tau(z) & z \geq z_1, \\ \tau(z) + \eta(z_1 - z)\sigma^{\text{ext}}_{\text{aer}} & z \in (z_0, z_1), \\ \tau(z) + \eta(z_1 - z_0)\sigma^{\text{ext}}_{\text{aer}} & z \leq z_0. \end{cases} \tag{6.9}$$

Now, write $I(\eta)$ and $I(0)$ for the top of atmosphere radiance corresponding to the perturbed and the unperturbed atmosphere, respectively. Then, we are interested in computing the semi-analytic derivative of the top of atmosphere radiance $\frac{\delta I}{\delta n}(z)$, given by

$$\frac{\delta^2 I}{\delta n \delta z}(z) := \frac{1}{z_1 - z_0} \lim_{\eta \to 0} \frac{1}{\eta} \left(I(\eta) - I(0) \right), \tag{6.10}$$

where z is the midpoint of (z_0, z_1). Here, we use the notation $\frac{\delta}{\delta z}$ to distinguish between a real derivative and the following construction.

Remembering the single scattering approximation solution (6.6), we have

$$I(\eta) = \sum_{i \in \Lambda} C_i \int_0^\infty \bar{k}^{\text{sca}}_i(z) e^{-M\bar{\tau}(z)} \mathrm{d}z, \tag{6.11}$$

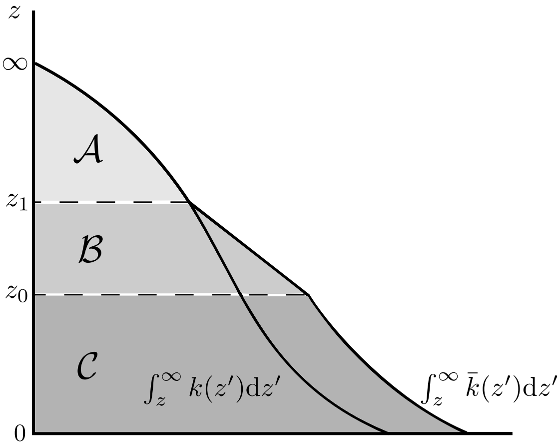

FIGURE 6.3: Schematic overview of the effect of a perturbation in aerosol number density on the optical depth variable. The perturbation in aerosol number density starts taking effect in domain $\mathcal{B}$ and this effect is exhausted starting from domain $\mathcal{C}$, after which the integrals only differ by a constant factor. Note that the profile of $k(z)$ has been taken arbitrarily, and the only thing that is important here is the cumulative property of the corresponding integrals.

with

$$C_i = \frac{E_0}{4\pi\mu} P_i(\mu, \phi, -\mu_0, \phi_0) \tag{6.12}$$

and

$$M = \frac{\mu + \mu_0}{\mu\mu_0} \tag{6.13}$$

is the *Geometric Airmass Factor*. Thus, we consider

$$\frac{1}{\eta}\left(I(\eta) - I(0)\right) = \sum_{i\in\Lambda} \frac{C_i}{\eta} \left[\int_0^\infty \bar{k}_i^{\mathrm{sca}}(z) e^{-M\bar{\tau}(z)}\mathrm{d}z - \int_0^\infty k_i^{\mathrm{sca}}(z) e^{-M\tau(z)}\mathrm{d}z\right]. \tag{6.14}$$

We split up the vertical profile into three domains over which we can distinguish different behavior for $\bar{\tau}$. These domains are given by $\mathcal{A} = (z_1, \infty)$, $\mathcal{B} = (z_0, z_1)$, and $\mathcal{C} = (0, z_0)$ (see Figure 6.3). The perturbation starts taking effect in domain $\mathcal{B}$ and this effect is exhausted starting from domain $\mathcal{C}$, but the perturbation still leaves its mark there, due to the cumulative property of $\bar{\tau}(z) = \int_z^\infty \bar{k}(z')\mathrm{d}z'$.

Splitting up the integrals over the three domains yields

$$\frac{1}{\eta}\left(I(\eta) - I(0)\right) = \sum_{i\in\Lambda} \frac{C_i}{\eta} \sum_{\mathcal{D}} \left[\int_{\mathcal{D}} \bar{k}_i^{\mathrm{sca}}(z) e^{-M\bar{\tau}(z)}\mathrm{d}z - \int_{\mathcal{D}} k_i^{\mathrm{sca}}(z) e^{-M\tau(z)}\mathrm{d}z\right], \tag{6.15}$$

where $\mathcal{D} \in \{\mathcal{A}, \mathcal{B}, \mathcal{C}\}$ for the second summation.

First, we treat the differences between brackets in (6.15) for the aerosol. Then, we deal with the contribution of the molecules.

For $z \in \mathcal{A}$, the perturbation has not had any effect yet, and all differences cancel, i.e.

$$\int_{\mathcal{A}} \bar{k}_{\text{aer}}^{\text{sca}}(z) e^{-M\bar{\tau}(z)} \mathrm{d}z - \int_{\mathcal{A}} k_{\text{aer}}^{\text{sca}}(z) e^{-M\tau(z)} \mathrm{d}z = 0. \tag{6.16}$$

Next, for $z \in \mathcal{C}$ we have that $\bar{k}_{\text{aer}}^{\text{sca}}(z) = k_{\text{aer}}^{\text{sca}}(z)$, and $\bar{\tau}(z) = \tau(z) + \eta(z_1 - z_0)\sigma_{\text{aer}}^{\text{ext}}$. Hence,

$$\begin{aligned} \int_{\mathcal{C}} \bar{k}_{\text{aer}}^{\text{sca}}(z) e^{-M\bar{\tau}(z)} \mathrm{d}z - \int_{\mathcal{C}} k_{\text{aer}}^{\text{sca}}(z) e^{-M\tau(z)} \mathrm{d}z &= \\ - \int_{\mathcal{C}} k_{\text{aer}}^{\text{sca}}(z) e^{-M\tau(z)} \left(1 - e^{-\eta M(z_1 - z_0)\sigma_{\text{aer}}^{\text{ext}}}\right) \mathrm{d}z&, \end{aligned} \tag{6.17}$$

where we have put the minus sign in front to accentuate the sign of this difference.

Finally, when $z \in \mathcal{B}$, we have $\bar{k}_{\text{aer}}^{\text{sca}}(z) = k_{\text{aer}}^{\text{sca}}(z) + \eta\sigma_{\text{aer}}^{\text{sca}}$, and $\bar{\tau}(z) = \tau(z) + \eta(z_1 - z)\sigma_{\text{aer}}^{\text{ext}}$. Thus,

$$\begin{aligned} &\int_{\mathcal{B}} \bar{k}_{\text{aer}}^{\text{sca}}(z) e^{-M\bar{\tau}(z)} \mathrm{d}z - \int_{\mathcal{B}} k_{\text{aer}}^{\text{sca}}(z) e^{-M\tau(z)} \mathrm{d}z = \\ &\int_{\mathcal{B}} \eta\sigma_{\text{aer}}^{\text{sca}} e^{-M(\tau(z) + (z_1 - z)\eta\sigma_{\text{aer}}^{\text{ext}})} \mathrm{d}z - \int_{\mathcal{B}} k_{\text{aer}}^{\text{sca}}(z) e^{-M\tau(z)} \left(1 - e^{-M(z_1 - z)\eta\sigma_{\text{aer}}^{\text{ext}}}\right) \mathrm{d}z. \end{aligned} \tag{6.18}$$

For molecules, we note that the only thing that is different, is that for $z \in \mathcal{B}$, we do not have additional (non aerosol) molecules due to the perturbation. Thus, the Rayleigh scattering coefficient remains unchanged in the perturbation, i.e. $\bar{k}_{\text{mol}}^{\text{sca}}(z) = k_{\text{mol}}^{\text{sca}}(z)$. As a consequence, we do not have a positive contribution due to added Rayleigh scattering. The negative contributions in domains $\mathcal{B}$ and $\mathcal{C}$ remain, though. These are terms that follow from a decrease in scattering due to a shielding of added aerosol, which can be traced back to the increase in the optical thickness, $\bar{\tau}$. Thus, we get

$$\begin{aligned} \int_{\mathcal{C}} \bar{k}_{\text{mol}}^{\text{sca}}(z) e^{-M\bar{\tau}(z)} \mathrm{d}z - \int_{\mathcal{C}} k_{\text{mol}}^{\text{sca}}(z) e^{-M\tau(z)} \mathrm{d}z &= \\ - \int_{\mathcal{C}} k_{\text{mol}}^{\text{sca}}(z) e^{-M\tau(z)} \left(1 - e^{-\eta M(z_1 - z_0)\sigma_{\text{aer}}^{\text{ext}}}\right) \mathrm{d}z&, \end{aligned} \tag{6.19}$$

and

$$\begin{aligned} \int_{\mathcal{B}} \bar{k}_{\text{mol}}^{\text{sca}}(z) e^{-M\bar{\tau}(z)} \mathrm{d}z - \int_{\mathcal{B}} k_{\text{mol}}^{\text{sca}}(z) e^{-M\tau(z)} \mathrm{d}z &= \\ - \int_{\mathcal{B}} k_{\text{mol}}^{\text{sca}}(z) e^{-M\tau(z)} \left(1 - e^{-\eta M(z_1 - z)\sigma_{\text{aer}}^{\text{ext}}}\right) \mathrm{d}z&, \end{aligned} \tag{6.20}$$

for the region $\mathcal{C}$ and $\mathcal{B}$, respectively. Note that in both cases the final exponent contains the aerosol extinction cross section because this is the constituent that is added, and leads to extra extinction.

Now that we have derived simple expressions for the difference quotients, we take the limit $\eta \to 0$. Naturally, we will treat this limit per domain $\mathcal{A}$, $\mathcal{B}$ and $\mathcal{C}$ separately as well.

For domain $\mathcal{A}$, the integrals canceled. Therefore, this domain has no contribution to the limit.

For domain $\mathcal{C}$, we consider the limit

$$\lim_{\eta \to 0} -\frac{1}{\eta}\left(1 - e^{-\eta(z_1 - z_0)\sigma_{\text{aer}}^{\text{ext}}}\right)\int_0^{z_0} k_i^{\text{sca}}(z) e^{-M\tau(z)}\mathrm{d}z. \tag{6.21}$$

Of course, the integral part is just some finite factor. If the integral was infinite there is no point in even trying to compute the derivative, as that would imply that the top of atmosphere radiance is infinite as well. Thus, we only need to compute

$$\lim_{\eta \to 0} -\frac{1}{\eta}\left(1 - e^{-\eta M(z_1 - z_0)\sigma_{\text{aer}}^{\text{ext}}}\right) = -M(z_1 - z_0)\sigma_{\text{aer}}^{\text{ext}}, \tag{6.22}$$

such that the final contributions due to domain $\mathcal{C}$ are given by

$$-M(z_1 - z_0)\sigma_{\text{aer}}^{\text{ext}}\int_0^{z_0} k_i^{\text{sca}}(z) e^{-M\tau(z)}\mathrm{d}z, \tag{6.23}$$

for both the aerosol and the molecules.

For domain $\mathcal{B}$, we need to treat two separate terms, which are given by

$$\frac{1}{\eta}\int_{z_0}^{z_1} \eta\sigma_{\text{aer}}^{\text{sca}} e^{-M\tau(z)} e^{-\eta a(z)}\mathrm{d}z = \int_{z_0}^{z_1} \sigma_{\text{aer}}^{\text{sca}} e^{-M\tau(z)} e^{-\eta a(z)}\mathrm{d}z, \tag{6.24}$$

for the positive aerosol contribution and

$$-\frac{1}{\eta}\int_{z_0}^{z_1} k_i^{\text{sca}}(z) e^{-M\tau(z)}\left(1 - e^{-\eta a(z)}\right)\mathrm{d}z, \tag{6.25}$$

for the negative contributions from both aerosol and molecules, where

$$a(z) = M(z_1 - z)\sigma_{\text{aer}}^{\text{ext}}. \tag{6.26}$$

Both terms will involve the interchange of the limit and integral operator, which we justify by using convergence theorems from Lebesgue integration theory. We can use these theorems provided that the Riemann integral that is obtained as a result exists (in which case it is equal to the Lebesgue integral). These two theorems, the *Monotone Convergence Theorem* (MCT) and the *Dominated Convergence Theorem* (DCT), are given in appendix A. There, we also give the theorem stating that the Lebesgue interals equal Riemann integrals if the Riemann integral exists.

The first case is easy. We need to show that

$$\lim_{\eta\to 0}\int_{z_0}^{z_1} \sigma_{\text{aer}}^{\text{sca}} e^{-M\tau(z)} e^{-\eta a(z)} \mathrm{d}z = \int_{z_0}^{z_1} \lim_{\eta\to 0} \sigma_{\text{aer}}^{\text{sca}} e^{-M\tau(z)} e^{-\eta a(z)} = \sigma_{\text{aer}}^{\text{sca}} \int_{z_0}^{z_1} e^{-M\tau(z)} \mathrm{d}z. \tag{6.27}$$

We are allowed to take the limit inside because of the DCT:

Take as a dominating function

$$g(z) = \sigma_{\text{aer}}^{\text{sca}} e^{-M\tau(z)}. \tag{6.28}$$

Then,

$$\sigma_{\text{aer}}^{\text{sca}} e^{-M\tau(z)} e^{-a(z)/n} \leq g(z) \tag{6.29}$$

for all z and n, because $e^{-a(z)/n} \leq 1$ for all $n > 0$, and $a(z) > 0$. Furthermore, we have that

$$\int_{z_0}^{z_1} g(z)\mathrm{d}z < \infty. \tag{6.30}$$

Thus, the DCT holds and therefore (6.27) as well.

The second case is very similar to the case for domain $\mathcal{C}$, except in this case we cannot take the factor $\left(1 - e^{-\eta a(z)}\right)$ out of the integral, due to its dependence on z. However, if we are allowed to bring the limit inside the integral, the approach is not much different, and the resulting limit is given by

$$\lim_{\eta\to 0} -\frac{1}{\eta}\int_{z_0}^{z_1} k_i^{\text{sca}}(z) e^{-M\tau(z)} \left(1 - e^{-\eta a(z)}\right) \mathrm{d}z = -\int_{z_0}^{z_1} a(z) k_i^{\text{sca}}(z) e^{-M\tau(z)} \mathrm{d}z, \tag{6.31}$$

since

$$\lim_{\eta\to 0}\frac{1}{\eta}\left(1 - e^{-\eta a(z)}\right) = a(z). \tag{6.32}$$

To prove we are allowed to exchange the integral and the limit operator, we use the MCT.

Consider the function

$$g_n(z) = k_i^{\text{sca}}(z) e^{-M\tau(z)} f_n(z), \tag{6.33}$$

where

$$f_n(z) = n\left(1 - e^{-a(z)/n}\right). \tag{6.34}$$

Note that these functions represent our integrands of interest modulo a minus sign, after transforming $n = 1/\eta$, such that the MCT is applicable.

Since $0 \leq k_i^{\mathrm{sca}}(z)e^{-M\tau(z)} < \infty$, and $n\left(1 - e^{-a(z)/n}\right) \geq 0$, the MCT holds whenever $f_n(z) \uparrow f(z)$ pointwise, and

$$\lim_{n\to\infty} f_n(z) = f(z) = a(z) \tag{6.35}$$

exists, which it obviously does.

We show that $f_n(z) \uparrow f(z)$ pointwise, or, since we know that the limit exists, that $f_{n+1}(z) \geq f_n(z)$ for all z. Therefore, we compute

$$\frac{\mathrm{d}}{\mathrm{d}n} f_n(z) = \frac{\mathrm{d}}{\mathrm{d}n} n\left(1 - e^{-a(z)/n}\right) = 1 - (1 + a(z)/n)e^{-a(z)/n}. \tag{6.36}$$

Now,

$$1 - (1 + a(z)/n)e^{-a(z)/n} \geq 0 \Leftrightarrow e^{a(z)/n} \geq 1 + a(z)/n, \tag{6.37}$$

and considering the Taylor expansion for $e^{a(z)/n}$,

$$e^{a(z)/n} = 1 + a(z)/n + \frac{(a(z)/n)^2}{2!} + \frac{(a(z)/n)^3}{3!} + ..., \tag{6.38}$$

this is certainly the case for $a(z) > 0$. This holds for all realistic parameter values. Hence, $\frac{\mathrm{d}}{\mathrm{d}n} f_n(z) \geq 0$, which implies $f_{n+1}(z) \geq f_n(z)$. This completes the proof, and indeed equation (6.31) holds.

Concluding, we have

$$\begin{aligned}
\lim_{\eta\to 0} \frac{1}{\eta}\left(I(\eta) - I(0)\right) &= C_{\mathrm{aer}}\sigma_{\mathrm{aer}}^{\mathrm{sca}} \int_{z_0}^{z_1} e^{-M\tau(z)}\mathrm{d}z & (6.39)\\
&- C_{\mathrm{aer}} M\sigma_{\mathrm{aer}}^{\mathrm{ext}} \int_{z_0}^{z_1} (z_1 - z)k_{\mathrm{aer}}^{\mathrm{sca}}(z)e^{-M\tau(z)}\mathrm{d}z & (6.40)\\
&- C_{\mathrm{aer}} M(z_1 - z_0)\sigma_{\mathrm{aer}}^{\mathrm{ext}} \int_{0}^{z_0} k_{\mathrm{aer}}^{\mathrm{sca}}(z)e^{-M\tau(z)}\mathrm{d}z & (6.41)\\
&- C_{\mathrm{mol}} M\sigma_{\mathrm{aer}}^{\mathrm{ext}} \int_{z_0}^{z_1} (z_1 - z)k_{\mathrm{mol}}^{\mathrm{sca}}(z)e^{-M\tau(z)}\mathrm{d}z & (6.42)\\
&- C_{\mathrm{mol}} M(z_1 - z_0)\sigma_{\mathrm{aer}}^{\mathrm{ext}} \int_{0}^{z_0} k_{\mathrm{mol}}^{\mathrm{sca}}(z)e^{-M\tau(z)}\mathrm{d}z. & (6.43)
\end{aligned}$$

This equation describes how much our top of atmosphere radiance, in direction (μ, ϕ), changes given some infinitesimal change in aerosol number density in the interval (z_0, z_1). In this derivative, we can distinguish several effects. First, due to an increased amount of aerosol at (z_0, z_1) there is an increase in scattering of photons towards the top of the atmosphere, which is represented in (6.39). Second, because we only track singly scattered photons, the extra photons that are scattered by the added aerosol are no longer available for scattering at any lower altitude by aerosol ((6.40) and (6.41)) or molecules ((6.42) and (6.43)).

To obtain the semi-analytic derivative $\frac{\delta^2 I}{\delta n \delta z}$, we only need to divide the expression above by the width of the perturbation interval, $z_1 - z_0$.

In conclusion, note that in order to actually compute the derivatives, we need to carry out numerical integrations over the altitude. Since all other quantities are already known, this can be done once the full optical thickness profile, $\tau(z)$, is computed.

6.4 Derivative of Measured Radiance

Above, we determined monochromatic (for each wavelength) derivatives. Of course, we are interested in the derivative for the *measured* radiance, i.e.

$$\frac{\delta \hat{I}}{\delta n}(z) = \frac{1}{z_1 - z_0} \lim_{\eta \to 0} \frac{1}{\eta} \left(\hat{I}(\lambda; \eta) - \hat{I}(\lambda; 0) \right), \tag{6.44}$$

where $\hat{I}(\lambda; \eta)$ and $I(\lambda; 0)$ are the measured radiances at wavelength λ (see section 5.6) for the perturbed atmosphere and normal atmosphere, respectively.

We claim that

$$\lim_{\eta \to 0} \frac{1}{\eta} \left(\hat{I}(\lambda; \eta) - \hat{I}(\lambda; 0) \right) = D(\lambda) \int_{\lambda_{\min}}^{\lambda_{\max}} S(\lambda, \lambda') \left[\lim_{\eta \to 0} \frac{1}{\eta} \left(I(\lambda; \eta) - I(\lambda; 0) \right) \right] \mathrm{d}\lambda', \tag{6.45}$$

i.e. to obtain the derivative of the measured radiance, we can consider the monochromatic radiance's derivative and perform the convolution with the instrument spectral response function afterwards.

To prove (6.45), we first note that, due to the linearity of the integral, the following holds:

$$\lim_{\eta \to 0} \frac{1}{\eta} \left(\hat{I}(\lambda; \eta) - \hat{I}(\lambda; 0) \right) = \lim_{\eta \to 0} \frac{1}{\eta} \left(D(\lambda) \int_{\lambda_{\min}}^{\lambda_{\max}} S(\lambda, \lambda') \left(I(\lambda'; \eta) - I(\lambda'; 0) \right) \mathrm{d}\lambda' \right), \tag{6.46}$$

since $I(\lambda'; \eta)$ and $I(\lambda'; 0)$ are integrable.

Now, we need to show that

$$\lim_{\eta \to 0} \int_{\lambda_{\min}}^{\lambda_{\max}} S(\lambda, \lambda') \frac{1}{\eta} \left(I(\lambda'; \eta) - I(\lambda'; 0) \right) \mathrm{d}\lambda' = \int_{\lambda_{\min}}^{\lambda_{\max}} S(\lambda, \lambda') \left[\lim_{\eta \to 0} \frac{1}{\eta} \left(I(\lambda'; \eta) - I(\lambda'; 0) \right) \right] \mathrm{d}\lambda'. \tag{6.47}$$

This proof concerns taking the limit inside the integral over the wavelength as well. Thus, we need to extend the arguments made in the previous section, such that they also incorporate the integral over the wavelength. Again, we can separate the arguments per region. We can also separate the arguments per atmospheric constituent, but we will only prove it for aerosol, as the arguments for molecules are identical.

First, for the $\mathcal{C}$ region, we note that the factor the limit considers can also be taken out of the outer integral (since $\sigma_{\text{aer}}^{\text{ext}}$ is assumed to be independent of λ). So for the $\mathcal{C}$ region, the argument is sound.

Second, for the first $\mathcal{B}$ part, we can use the DCT again. Consider the dominating function

$$g(\lambda, \lambda') = \sigma_{\text{aer}}^{\text{sca}} S(\lambda, \lambda') C_{\text{aer}}(\lambda') \int_{z_0}^{z_1} e^{-M\tau(z,\lambda')} \mathrm{d}z. \tag{6.48}$$

This function dominates the integrand because $e^{-M\sigma_{\text{aer}}^{\text{ext}}(z_1 - z)/n} \leq 1$. Furthermore, it is obvious that $\int g(\lambda, \lambda')\mathrm{d}\lambda'$ is finite. Thus, the DCT holds.

Finally, for the second $\mathcal{B}$ part, we note that we can use the same MCT, but we need to be a bit more careful: We need to prove that

$$\lim_{n\to\infty} \int_{\lambda_{\min}}^{\lambda_{\max}} h_n(\lambda, \lambda')\mathrm{d}\lambda' = \int_{\lambda_{\min}}^{\lambda_{\max}} \lim_{n\to\infty} h_n(\lambda, \lambda')\mathrm{d}\lambda', \tag{6.49}$$

where

$$h_n(\lambda, \lambda') = S(\lambda, \lambda') C_{\text{aer}}(\lambda') \int_{z_0}^{z_1} k_{\text{aer}}^{\text{sca}}(z) e^{-M\tau(z,\lambda')} f_n(z, \lambda')\mathrm{d}z, \tag{6.50}$$

where $f_n(z)$ is the monotone sequence of functions from the previous section.

Note that we already know that $\lim_{n\to\infty} h_n(\lambda, \lambda')$ exists, because of our work for the monochromatic derivative.

Next, it is very easy to show that $h_{n+1} \geq h_n$. We already showed that

$$f_{n+1}(z, \lambda') - f_n(z, \lambda') \geq 0. \tag{6.51}$$

Hence,

$$h_{n+1} - h_n = S(\lambda, \lambda') C_{\text{aer}}(\lambda') \int_{z_0}^{z_1} k_{\text{aer}}^{\text{sca}}(z) e^{-M\tau(z,\lambda')} \left(f_{n+1}(z, \lambda') - f_n(z, \lambda')\right) \mathrm{d}z \geq 0, \tag{6.52}$$

since all other factors are positive as well. Therefore, $h_{n+1} \geq h_n$, and we can use the MCT and take the limit inside.

In conclusion, we have shown that we can find the derivative of the measured radiance by first computing the derivative of the monochromatic radiance, and then convolving the monochromatic derivatives with the instrument spectral response function.

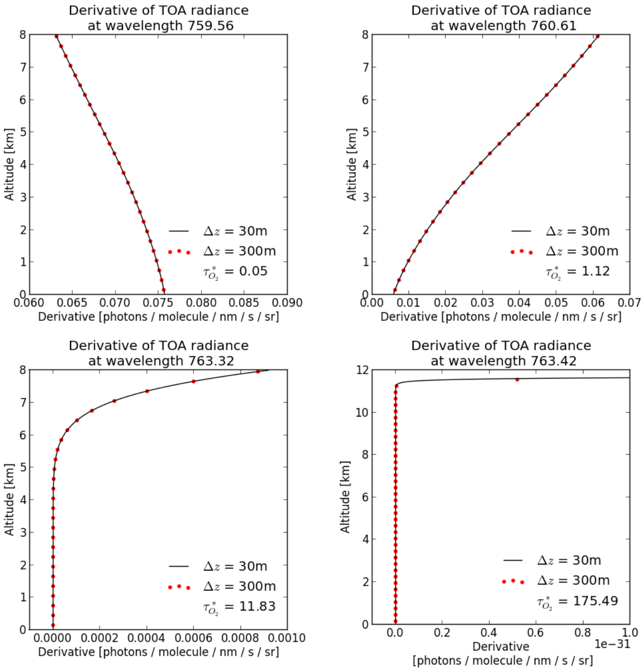

FIGURE 6.4: Monochromatic derivatives for the SAT region at wavelengths $\lambda = 759.56$ nm (top left), $\lambda = 760.61$ nm (top right), $\lambda = 763.32$ nm (bottom left), and $\lambda = 763.42$ nm (bottom right). The corresponding O_2 absorption optical thicknesses, $\tau^*_{O_2}$, are 0.05, 1.12, 11.83, and 175.49, respectively. The derivatives are shown for two different perturbation thicknesses $\Delta z = 30$m (black) and $\Delta z = 300$m (red). Note that for the wavelength with highest optical thickness (bottom right), the axes are different.

6.5 Computing Derivatives

The semi-analytic derivatives hold for the particular atmospheric layer in which we perturb the aerosol number density, i.e. the layer located at (z_0, z_1). To obtain the derivative for the entire atmosphere, we need to compute derivatives for a sequence of layers.

The thinner the perturbation layer, the more accurate the derivative. Furthermore, derivatives based on small perturbation thicknesses ($\Delta z = z_1 - z_0$) are also able to reveal more detail. However, decreasing the thickness also increases the amount of layers required to cover the atmosphere, and thus computation time. We decide to investigate the dependency on the perturbation thickness in more detail.

Figure 6.4 shows the computed derivatives for the SAT region at three wavelengths for two different thicknesses of the perturbation layer, $\Delta z = 30$m and $\Delta z = 300$m, and for increasing O_2 absorption optical thickness. We see that the general behavior of the derivatives are consistent for both thicknesses.

We conclude that there is no strong dependence on the perturbation thickness Δz. However, detail is lost when the thickness is increased. Since we do not care for computation

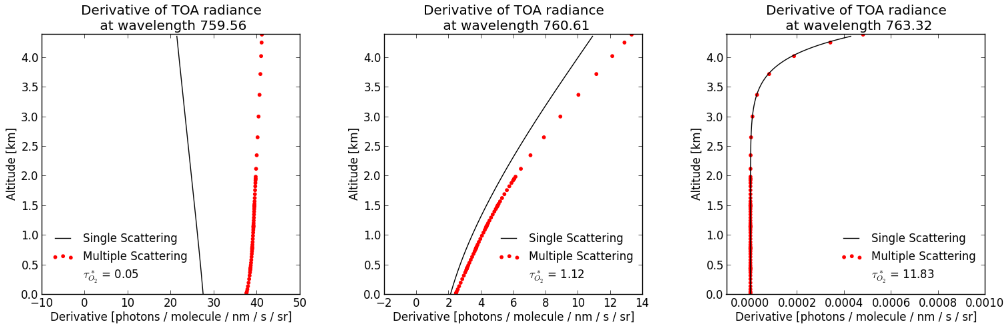

Figure 6.5: Monochromatic derivatives for the SPA region at wavelengths $\lambda = 759.56$ nm (left), $\lambda = 760.61$ nm (center), and $\lambda = 763.32$ nm (right). The corresponding O_2 absorption optical thicknesses, $\tau^*_{O_2}$, are 0.05, 1.12, and 11.83, respectively. The derivatives are shown for the single scattering (black) and for multiple scattering (red).

time during this research, we decide to work with a small perturbation thickness. Thus, in the following we only use $\Delta z = 30$m. Whenever computation time does become an issue, this thickness can always be increased at the cost of a decrease in detail.

Next, we compare the derivatives of the single scattering approximation to multiple scattering derivatives as computed by DISAMAR. In appendix B we describe how we obtain these multiple scattering derivatives.

Figure 6.5 shows the derivatives for the SPA scene for three wavelengths, with increasing O_2 absorption optical thickness. The fourth wavelength that was also shown in 6.4 was left out this time, because the derivatives were extremely small (10^{-180}) at the altitudes where we can obtain a derivative with DISAMAR (i.e. an altitude where we still have aerosol). We picked the SPA scene because this scene showed the best approximation in section 6.2, so this can be seen as a best case scenario. However, we got similar results for the other scenes, except for a few continental scenes where the multiple scattering derivatives became negative due to shielding effects (not shown).

For the low absorption case, we see that the derivatives of the approximation have an error up to 50%, which is quite large. For the higher absorption cases, we see that the approximation performs much better. We see that the approximation increases in accuracy as we increase the O_2 absorption optical thickness. This is in correspondence with was observed in section 6.2.

Finally, we compute, and show, the derivatives of the measured top of atmosphere radiance for two representative scenes as a function of wavelength and altitude of the perturbation layer in Figure 6.6.

We see a strong dependence on the O_2 absorption optical thickness. The derivatives are relatively small in the strong absorption parts at low altitudes. Furthermore, inside the strong absorption parts, the derivatives are strictly increasing with altitude. We

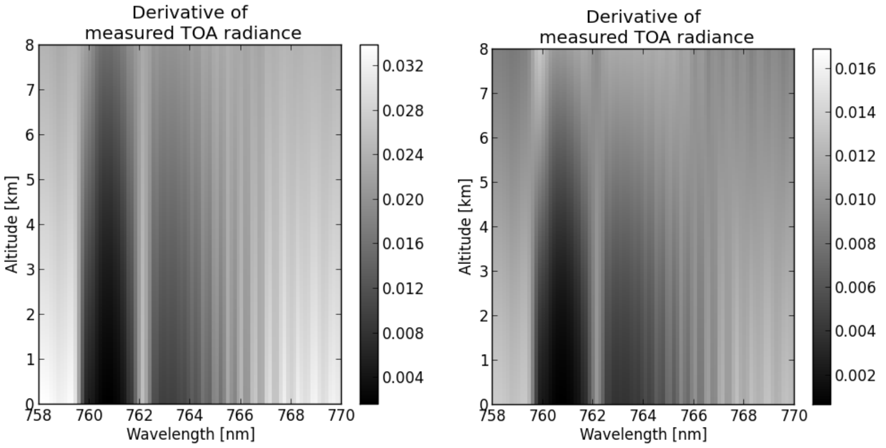

FIGURE 6.6: Measured top of atmosphere radiance derivatives as a function of wavelength and altitude of the perturbation layer. A darker color means that the derivative is smaller. The depicted scenes are SAT (left) and ECI (right).

conclude that, inside the absorption band, the top of atmosphere radiance is less sensitive to aerosol in the lower part of the atmosphere. This insensitivity gets progressively worse as we increase the strength of the O_2 absorption. However, although the top of atmosphere radiance can become insensitive when absorption is too strong, especially these wavelengths are very valuable as their derivatives also vary strongly with altitude, which we need to be able to obtain height information.

6.6 Extensions

We can attempt to extend the single scattering approximation to also incorporate the surface, or include second or higher orders of scattering. First we discuss including the surface, and then we discuss additional orders of scattering.

When we attempt to incorporate the surface, we get the additional source term S_b, see (4.29). This source term depends on the solution at the surface, $I^{\downarrow}(\tau^*, \mu, \phi)$, which is problematic. One can try to avoid this problem by making an approximation of the downward radiance at the surface.

An obvious approximation to the solution at the surface, would be to ignore the scattered contribution, which is reasonable under a low scattering optical thickness, and consider only the direct part of the solution, i.e.

$$I^{\downarrow}(\tau^*, \mu, \phi) \approx E_0 e^{-\tau^*/\mu_0} \delta(\mu - \mu_0) \delta(\phi - \phi_0). \tag{6.53}$$

This then yields the approximated surface source term

$$S_b(\tau,\mu,\phi) \approx \frac{\omega(\tau)}{4\pi}\frac{A_s E_0}{\pi} e^{-\tau^*/\mu_0} \int_0^{2\pi}\int_0^1 P(u,\phi,\mu',\phi') e^{-(\tau^*-\tau)/\mu'} \mathrm{d}\mu'\mathrm{d}\phi'. \qquad (6.54)$$

Now, since this expression no longer depends on the solution, the solution can be derived by integrating the source function over the height variable, as described in section 4.3. Unfortunately, we are generally unable to evaluate the double integral (6.54) analytically. We have experienced that solving for the top of atmosphere radiance now becomes a problem with significantly increased numerical complexity.

Additionally, computing derivatives with the included surface term becomes troublesome, as they include terms with the integral

$$\int_0^{2\pi}\int_0^1 \frac{1}{\mu'} P(u,\phi,\mu',\phi') e^{-(\tau^*-\tau)/\mu'} \mathrm{d}\mu'\mathrm{d}\phi', \qquad (6.55)$$

which is even harder to compute numerically than the integral in (6.54), due to the extra factor $\frac{1}{\mu'}$.

Including additional orders of scattering is difficult because the multiple scattering source term (the final term in (4.28)) depends on the solution itself. We can however employ a Lambda iteration method (see [17]) to express the radiance as the sum of contributions $I_0, I_1, ..., I_n$ where I_n is the contribution to the radiance due to photons that are scattered n times. Then, using I_{n-1} in the source term for I_n yields a system of $n+1$ equations that we can solve. Not only is this construction quite complex, but this system of equations is only relatively easy to solve under the assumption of isotropic phase functions (i.e. no angular dependence of the scatterers).

Concluding, although it is possible to extend the single scattering approximation that is discussed in this chapter, it is not very advantageous to do so, as any extension will lead to a strong increase in numerical and mathematical complexity. Since we decided to use the single scattering approximation for its simplicity, trying to extend the approximation now makes little sense. When one needs to incorporate the surface or increase more order of scattering, full radiative transfer models, like DISAMAR's LABOS or the Doubling/Adding method, deal with these extensions in a much more efficient way.

Chapter 7

Interpretation of Retrieved Aerosol Layer Height

7.1 Introduction

We hypothesize that the Aerosol Layer Height solution for a realistic aerosol profile (see chapter 3) can be interpreted as a centroid of the aerosol profile, i.e. a weighted average of the aerosol profile, with proper weights. Here, we investigate this hypothesis by constructing centroids of the aerosol extinction profile.

This idea is inspired by [12], where centroids for cloud profiles are developed and compared to the Ozone Monitoring Instrument (OMI) cloud height product. These centroids use knowledge on the properties of the radiation field for cloudy atmospheres. These atmospheres typically have very diffuse light. For cloud free atmospheres with aerosols we need to consider other properties of the radiation field. Thus, we construct three different centroid methods.

These centroids can be computed without actually performing any retrieval simulations. This has the additional advantage that these methods can also be used in large scale validation studies if there is good agreement with the retrieval solution.

7.2 Basic Centroid

First, the most straightforward way to compute a centroid of the profile, is to integrate the altitude using the aerosol extinction profile as weights. Thus, we compute the centroid $\mathcal{Z}_{\text{basic}}(k_{\text{aer}}^{\text{ext}}(z))$ as follows:

$$\mathcal{Z}_{\text{basic}}(k_{\text{aer}}^{\text{ext}}(z)) = \frac{\int_0^\infty z k_{\text{aer}}^{\text{ext}}(z)\mathrm{d}z}{\int_0^\infty k_{\text{aer}}^{\text{ext}}(z)\mathrm{d}z}. \tag{7.1}$$

7.3 Centroid Based on Multiple Scattering Derivatives

Aerosol at different altitudes can have a significantly different impact on the top of atmosphere radiance (see section 6.5), and the retrieval solution may account for this fact. Thus, we also construct a centroid where we take into account the sensitivity of the top of atmosphere radiance to aerosol at a particular altitude. We compute a weighted average of the altitude, using as weights the product of the aerosol extinction coefficients and the measured top of atmosphere radiance derivative with respect to the aerosol number density. These multiple scattering derivatives are computed with DISAMAR. How we do this is described in appendix B.

The centroid $\mathcal{Z}_{\text{multiple}}(k_{\text{aer}}^{\text{ext}}(z), \lambda)$ is now computed as follows

$$\mathcal{Z}_{\text{multiple}}(k_{\text{aer}}^{\text{ext}}(z), \lambda) = \frac{\int_0^\infty z k_{\text{aer}}^{\text{ext}}(z) \left| \frac{\mathrm{d}^2\hat{I}}{\mathrm{d}n\mathrm{d}z}(z,\lambda) \right| \mathrm{d}z}{\int_0^\infty k_{\text{aer}}^{\text{ext}}(z) \left| \frac{\mathrm{d}^2\hat{I}}{\mathrm{d}n\mathrm{d}z}(z,\lambda) \right| \mathrm{d}z}, \tag{7.2}$$

where $\frac{\mathrm{d}^2\hat{I}}{\mathrm{d}n\mathrm{d}z}$ is the multiple scattering derivative of the measured radiance, as computed by DISAMAR. Since a strong negative derivative still means that the aerosol has a strong effect on the top of atmosphere radiance, we take the absolute value. Note that this is now a spectral quantity, due to the spectral dependence of $\frac{\mathrm{d}^2\hat{I}}{\mathrm{d}n\mathrm{d}z}$.

7.4 Centroid Based on Single Scattering Derivatives

Third, we again compute the centroid as before, using as weights the product of the aerosol extinction coefficient and the derivative of the measured top of atmosphere radiance. This time, however, we use the derivatives from the single scattering approximation, $\frac{\delta^2\hat{I}}{\delta n\delta z}$, as derived in chapter 6.

Thus, we define the centroid $\mathcal{Z}_{\text{single}}(k_{\text{aer}}^{\text{ext}}(z), \lambda)$ as

$$\mathcal{Z}_{\text{single}}(k_{\text{aer}}^{\text{ext}}(z), \lambda) = \frac{\int_0^\infty z k_{\text{aer}}^{\text{ext}}(z) \frac{\delta^2\hat{I}}{\delta n\delta z}(z,\lambda)\mathrm{d}z}{\int_0^\infty k_{\text{aer}}^{\text{ext}}(z) \frac{\delta^2\hat{I}}{\delta n\delta z}(z,\lambda)\mathrm{d}z}. \tag{7.3}$$

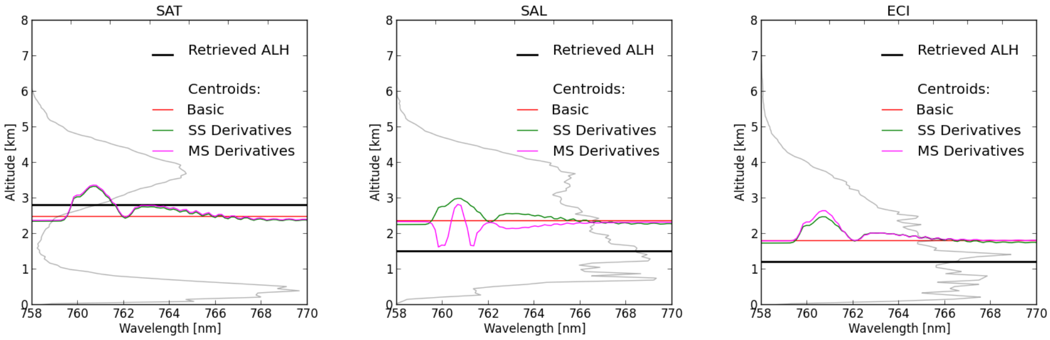

Figure 7.1: Centroids as a function of wavelength compared to the retrieved Aerosol Layer Height. The scenes that are shown are SAT (left), SAL (middle), and ECI (right). The dark black line is the retrieved Aerosol Layer Height, and the colored lines belong to the centroids, where red is the basic centroid $\mathcal{Z}_{\text{basic}}$, green is the centroid based on the single scattering derivatives $\mathcal{Z}_{\text{single}}$, and pink is the centroid based on the multiple scattering derivatives $\mathcal{Z}_{\text{multiple}}$. The true aerosol extinction profile is shown in gray.

This time, there is no need to take the absolute value of the derivative, because these are non-negative. Again, like the other centroid based on the multiple scattering derivatives, the centroid in (7.3) is also a spectral quantity.

7.5 Comparison

Figure 7.1 shows the computed centroids as a function of wavelength for the SAT, SAL and ECI scenes.

We see that all centroid methods exhibit some agreement with the retrieved Aerosol Layer Height, but none of the methods is of a clear higher quality than the others.

For the centroids based on the single scattering derivatives, we see an increase in centroid height inside the strong absorption parts of the O_2 A band. This is as expected, since the instrument is more sensitive to aerosol higher in the atmosphere, for those wavelengths (see section 6.5).

For the centroids based on the multiple scattering derivatives, the previous need not be the case. While we do see similar behavior for the SAT scene, the SAL scene actually shows a decrease in centroid altitude in some strong parts of the absorption band. This can be caused by, for example, shielding effects.

When the centroids based on the single scattering and multiple scattering derivatives agree, they do so very strongly. Indeed, we see for the SAT scene that these two centroid methods yield almost exactly the same results.

We also see that including information from derivatives need not improve the centroid method. For the ECI scene, we see that the basic centroid lies below the centroids of those based on the single scattering derivatives for a large part of the spectrum. Since the retrieved Aerosol Layer Height also lies below these centroids, the basic centroid might be preferred.

Finally, we note that the centroids based on the derivatives are spectral quantities. In order to properly compare these methods to retrieved Aerosol Layer Height, we need to combine the spectral information into a single quantity. We address this is the following section.

7.6 Spectral Averaging

We saw that the centroids based on the derivatives are spectral quantities. We need to combine the spectral information of these centroids to obtain a single quantity which can be compared to the retrieval solution.

We do not use the information from the entire wavelength window, since some of the spectral channels contain the same information, e.g. the continuum channels below 759 nm and above 768 nm.

Like in the cloud product Fast Retrieval Scheme for Clouds from the Oxygen A band (FRESCO), we use the information from three wavelength windows; 758-759 nm (continuum, no absorption), 760-761 nm (strong absorption), and 765-766 nm (moderate absorption), see [9]. The reflectivities in these three wavelength windows contain nearly all independent information that is available in the O_2 A band.

For the wavelengths within the previously described windows we again take a weighted average. We average the centroids over the wavelengths with the instrument's signal-to-noise ratio as weights.

7.7 Results

Computing the centroids after spectral averaging yields the results as presented in Figure 7.2. We see that all centroid methods yield similar results, but small difference are present. We investigate the individual performance of the three centroid methods.

Correlation graphs of each centroid method versus the retrieved Aerosol Layer Height are given in Figure 7.3. Furthermore, Pearson correlation coefficients r are also given.

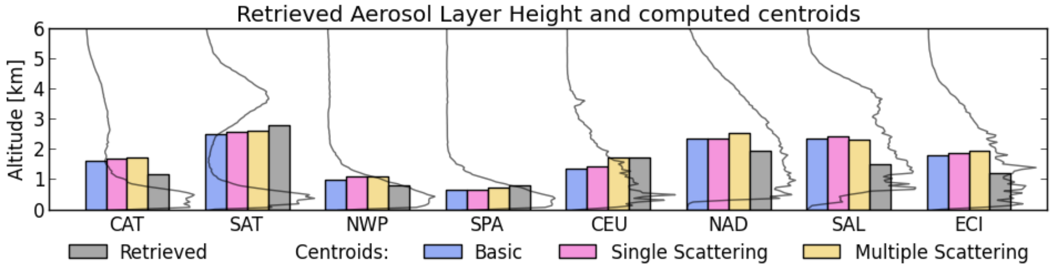

Figure 7.2: Bar diagram comparing computed centroids and the retrieved Aerosol Layer Height for all test scenes. The different centroid methods are distinguished via color. Retrieved Aerosol Layer Height is shown in gray, as is the corresponding extinction profile.

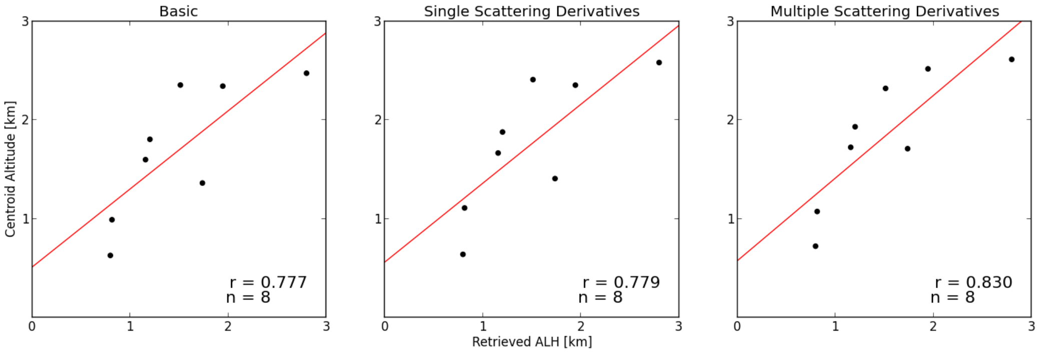

Figure 7.3: Correlation graphs for the three centroid methods versus the retrieved Aerosol Layer Height ($n = 8$). The centroid method based on the definition is on the left, while centroids based on the derivatives of the single- and multiple scattering approximations are given in the middle and to the right, respectively. The red line is a linear least-squares fit of the data.

We see that all centroid methods exhibit a fairly strong correlation with the retrieved Aerosol Layer Height ($n = 8$).

The correlation between the centroid methods and the retrieved Aerosol Layer Height further motivates our hypothesis that the retrieved Aerosol Layer Height can be interpreted as a centroid of the extinction profile. For the current dataset, the results suggest that the centroid method based on the multiple scattering derivatives is the best, as it shows the highest correlation.

A larger dataset of aerosol profiles is needed to improve the statistical power of the arguments made here. The ESA project Lidar Climatology of Vertical Aerosol Structure for Space-Based Lidar Simulation Studies (LIVAS), see [34], can be used to extend our dataset. This web portal provides an extensive aerosol profile database for remote sensing simulations, which are produced from CALIOP data in a similar fashion as in chapter 3.

If the centroid methods still show good agreement with the retrieved Aerosol Layer Height for a larger dataset, then we can use the centroid methods to compute quantities that are representative of the retrieved Aerosol Layer Height, without actually having to perform a retrieval simulation. This allows us to perform large scale validation studies, as seen in [12].

Chapter 8

Retrieval Revisited

8.1 Introduction

We have found evidence that the retrieval solution of the Aerosol Layer Height algorithm can be interpreted as a centroid of the aerosol extinction profile, provided that we only fit the optical thickness and the mid pressure of the aerosol layer. The default Aerosol Layer Height algorithm also fits the surface albedo. It does this, because the surface albedo is not known accurately: climatologies typically give monthly averages, but the variability is quite large on this time scale. For example, snowfall and changes in vegetation cover influence the reflectivity of the surface significantly. In this chapter, we investigate whether our previous results can be extended to the case where we also fit the surface albedo.

8.2 Including Surface Albedo

We perform the same simulation experiment as in section 3.3, except this time we also fit the surface albedo at 758 and 770 nm. All prior values, except for the mid pressure, equal their true values. We do not introduce any errors in the model parameters. The prior standard deviations equal 1 for the surface albedo nodes and the optical thickness, and for the mid pressure we set it at 500 hPa. We vary the prior mid pressure of the aerosol layer from 400 to about 900 hPa. Furthermore, we also vary the fixed pressure-thickness of the aerosol layer, with values $\Delta P = 50$ hPa, $\Delta P = 100$ hPa , $\Delta P = 200$ hPa, and $\Delta P = 300$ hPa. We repeat the same experiment for all scenes given in section 3.2.

The retrieval results for the scenes above sea (CAT, SAT, NWP and SPA) are given in Figure 8.1. The retrieval results for two of the land scenes, CEU and SAL, are given in Figure 8.2. The retrievals for the other two land scenes are not shown because these did not converge, as they reached the maximum number of iterations. Based on the retrieval results, the following observations can be made.

- All scenes show convergence issues. Most of these convergence issues occur when the a priori pressure is close to the surface and ΔP is large. In these cases, we often see that the algorithm stops on the boundary (the surface).
- Two continental scenes, NAD and ECI, show no convergence at all. For these regions, the intermediate solution oscillates between a solution with a high and a low aerosol layer. The high aerosol layer has a low optical thickness and a high surface albedo, while the low aerosol layer has a high optical thickness and a low surface albedo.
- When a solution is found, we see, in most cases, that the retrieved parameters are very stable as a function of the prior mid pressure, indicating that we are dealing with global minima.
- The SPA scene exhibits many minima, and hence unstable retrievals. It should be noted, however, that the SPA scene is the scene with the least amount of aerosol extinction, so the aerosol signal is relatively weak.
- Although small, we see variations in retrieval results for different values of the pressure thickness.
- For the scenes above sea, we retrieve exceptionally high mid pressures, accompanied by a low optical thickness and a high surface albedo. Except for the SAT scene, the retrieved mid pressure is even far above the aerosol profile. Although the mid pressure for the SAT scene is placed inside the aerosol profile, it is still comparatively higher than the mid pressure found in the retrievals of chapter 3.
- For the two continental scenes that show convergence, we observe different behavior than for the sea scenes. For the CEU scene, only the optical thickness is overestimated, while the other parameters are close to the (true) values retrieved in chapter 3. For the SAL scene, the mid pressure is overestimated, and both the optical thickness and surface albedo are underestimated.

This experiment has shown that retrieval results tend to be stable, whenever there is convergence. However, retrieval results that are found can be unrealistic. The next experiment further investigates these unrealistic retrievals.

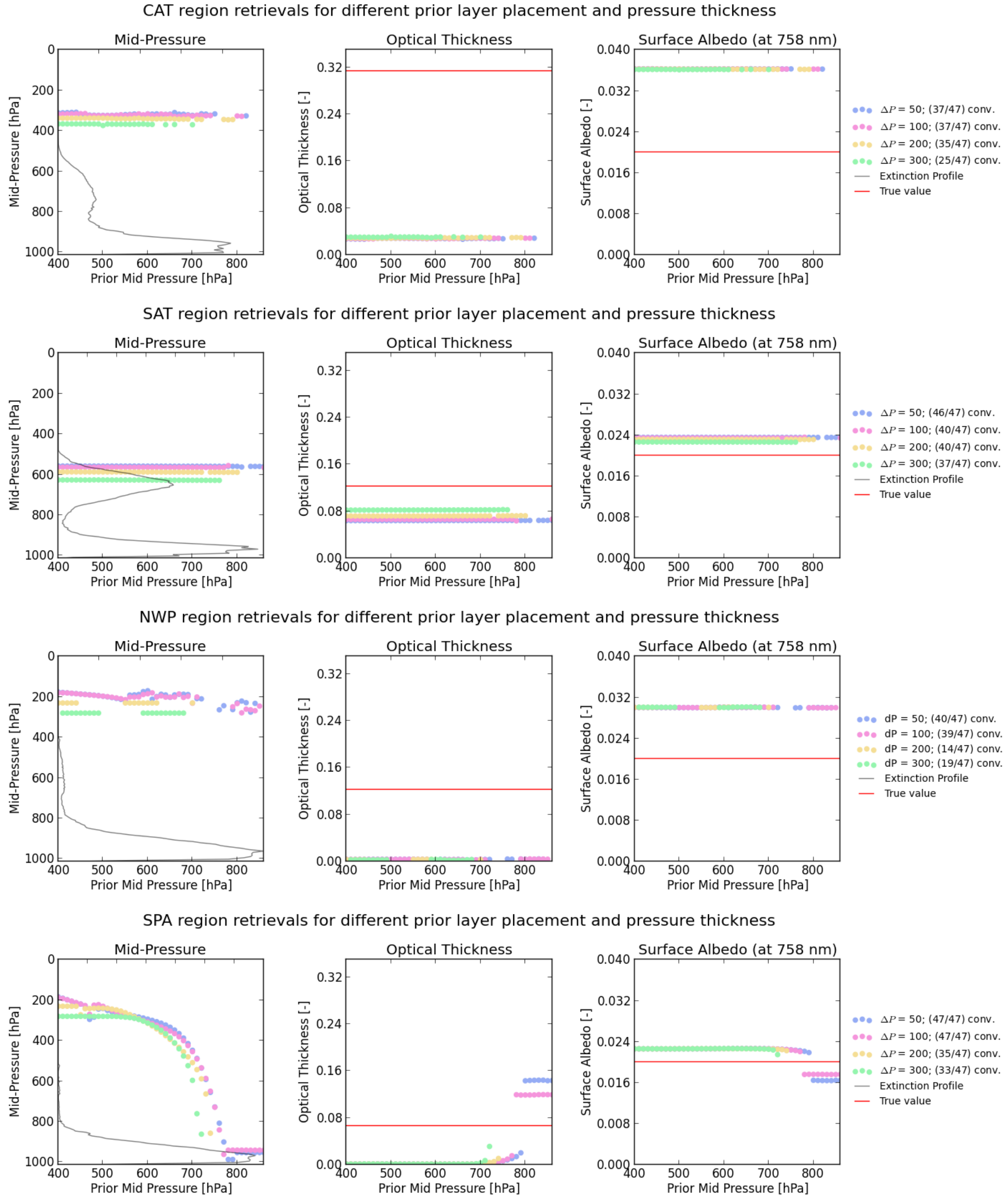

Figure 8.1: Retrieved parameters as a function of the a priori aerosol layer mid pressure for all four sea scenes. Fit parameters are mid pressure (left), optical thickness (middle), surface albedo at 758 nm (right), and surface albedo at 770 nm (not shown). The four scenes are the sea scenes CAT (first row), SAT (second row), NWP (third row), and SPA (fourth row). The four colors correspond to different pressure thicknesses, ΔP. The true extinction profiles are shown in gray (on an arbitrary linear scale), and the true optical thickness and surface albedo values are shown in red. A missing data point indicates a non-convergent retrieval, and convergence ratios are shown in the legend.

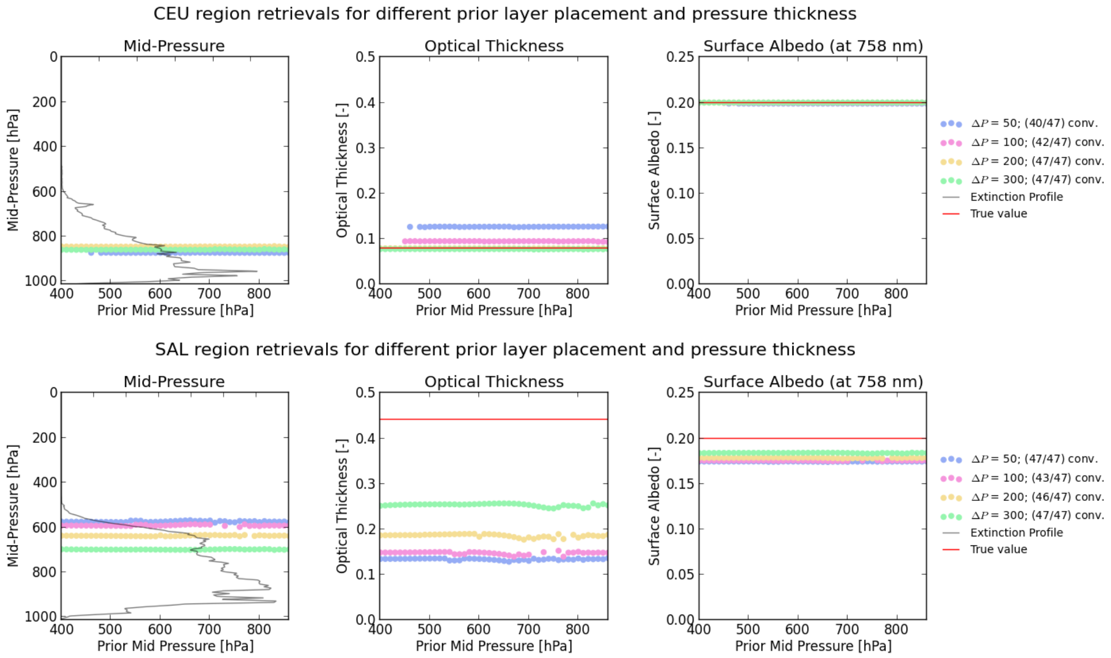

FIGURE 8.2: Retrieved parameters as a function of the a priori aerosol layer mid pressure for two land scenes. Fit parameters are mid pressure (left), optical thickness (middle), surface albedo at 758 nm (right), and surface albedo at 770 nm (not shown). The two scenes are the land scenes CEU (top) and SAL (bottom). The other two scenes are not displayed because the retrievals did not converge. The four colors correspond to different pressure thicknesses, ΔP. The true extinction profiles are shown in gray (on an arbitrary linear scale), and the true optical thickness and surface albedo values are shown in red. A missing data point indicates a non-convergent retrieval, and convergence ratios are shown in the legend.

8.3 Bifurcations

This retrieval experiment further investigates the unrealistic results that are obtained when the surface albedo is also retrieved.

We set the prior value of the surface albedo on its true value, and do retrievals for various values of the prior variance of the surface albedo, $\mathrm{Var}\,(A_s)$. We set the variance to values ranging from 10^{-7} to 1 (with 50 logarithmic steps). A prior variance of 0 would mean that we do not fit the surface albedo. The initial placement of the aerosol layer does not matter much, since we tend find global minima, as long as we do not start too close to the surface and the assumed pressure thickness is not too high. Therefore, we pick an aerosol layer that is initially placed at 620 hPa with a pressure thickness of $\Delta P = 100$ hPa.

The retrieval results for the sea scenes are shown in 8.3, and the results for the land scenes are shown in Figure 8.4. The following observations can be made.

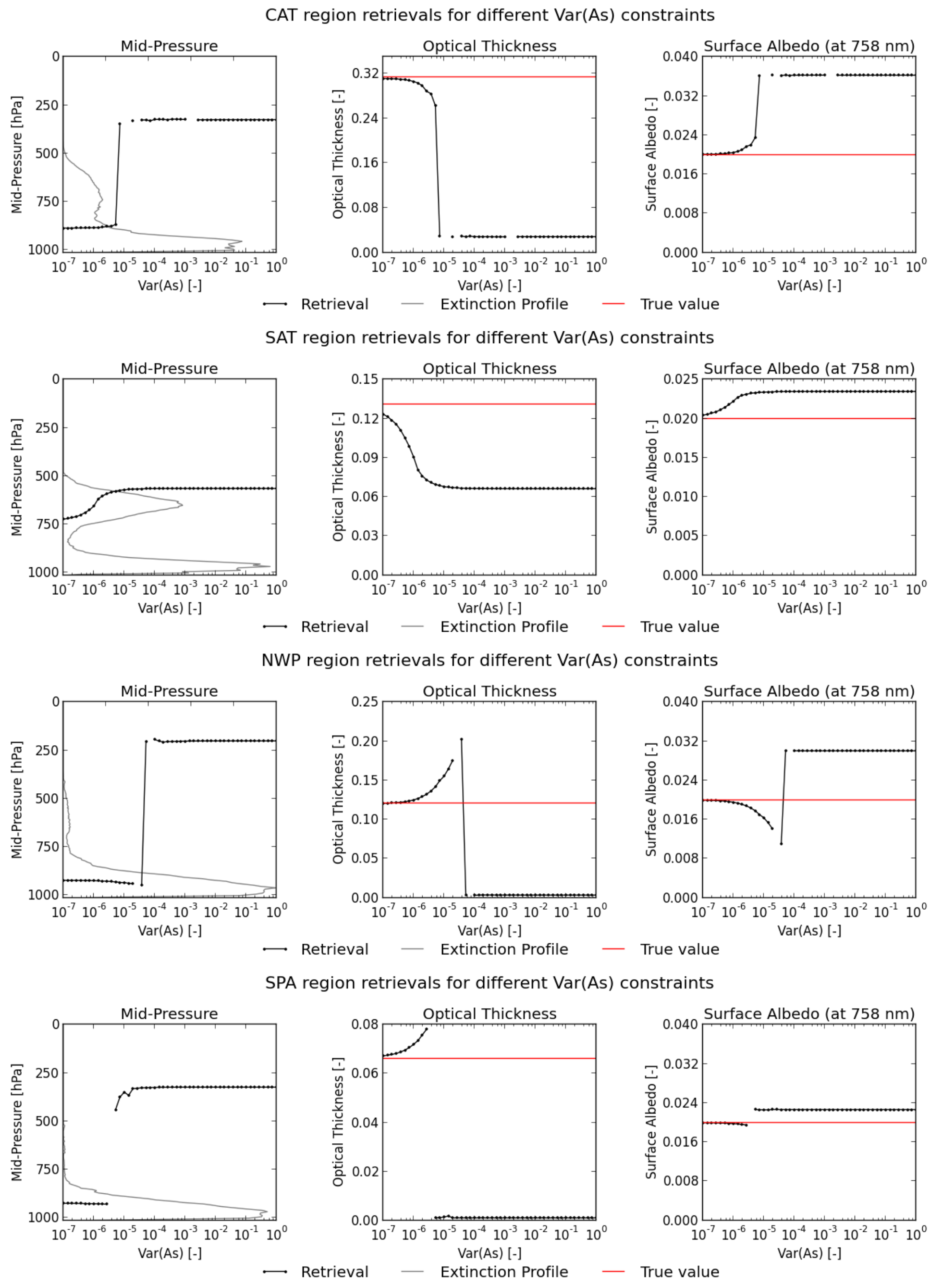

Figure 8.3: Retrieved parameters as a function of the a priori surface albedo variance, Var (A_s), for all four sea scenes. Fit parameters are mid pressure (left), optical thickness (middle), surface albedo at 758 nm (right), and surface albedo at 770 nm (not shown). The four scenes are the sea scenes CAT (first row), SAT (second row), NWP (third row), and SPA (fourth row). The retrieved parameters are shown in black and the true value is shown in red for the optical thickness and surface albedo. The true extinction profile is shown in gray on an arbitrary linear scale. Missing data points indicate non-convergence. Note the logarithmic scale for Var (A_s).

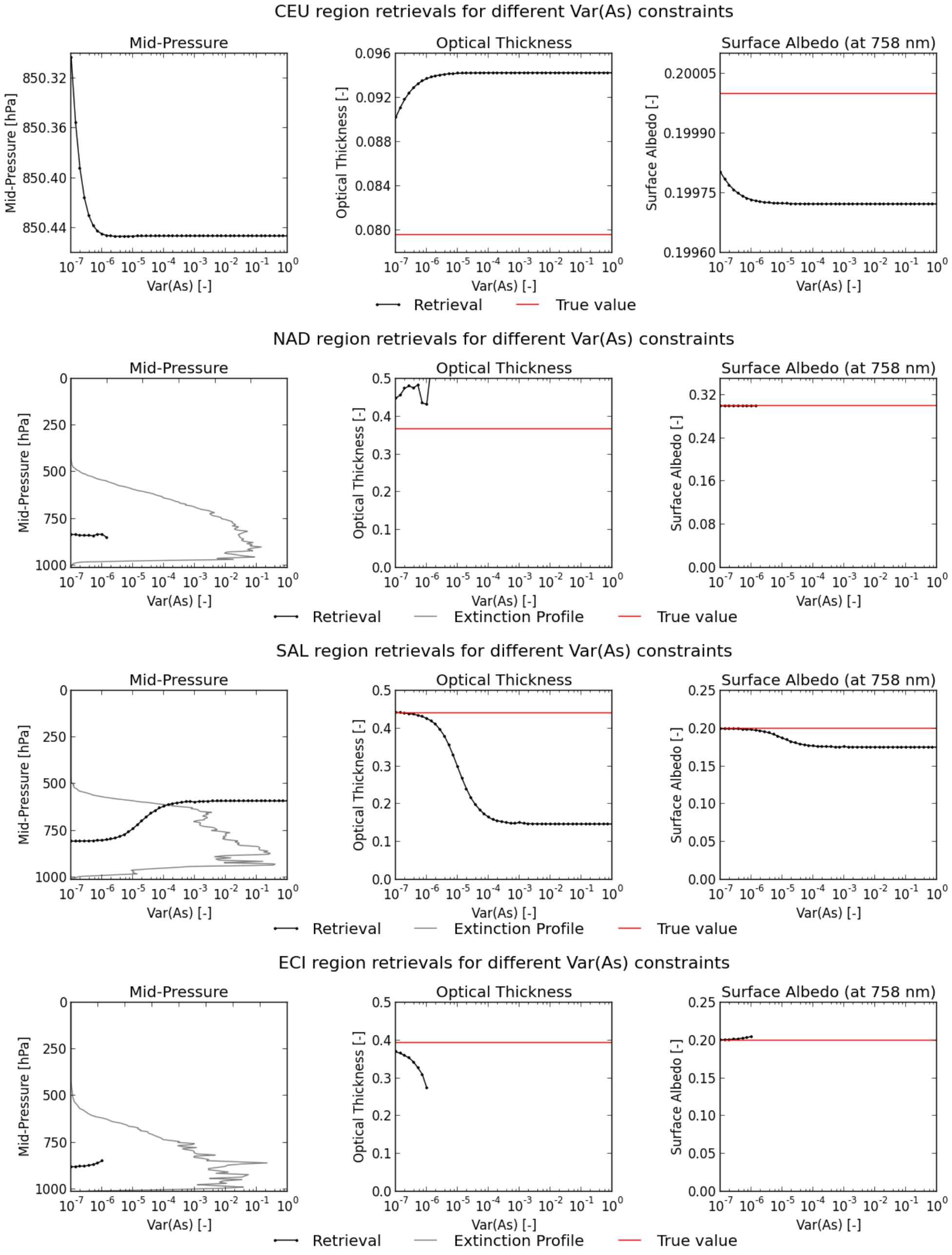

FIGURE 8.4: Retrieved parameters as a function of the a priori surface albedo variance, $\text{Var}(A_s)$, for all four land scenes. Fit parameters are mid pressure (left), optical thickness (middle), surface albedo at 758 nm (right), and surface albedo at 770 nm (not shown). The four scenes are the land scenes CEU (first row), NAD (second row), SAL (third row), and ECI (fourth row). The retrieved parameters are shown in black. The true extinction profile is shown in gray (arbitrary linear scales) and the true values for the optical thickness and surface albedo are shown in red. Missing data points indicate non-convergence. Note the logarithmic scale for $\text{Var}(A_s)$, and the compact y-axes for the CEU scene.

- For very small values of $\mathrm{Var}\,(A_s)$, we retrieve the same solution as when we do not fit the surface albedo. See chapter 3.
- A sharp change in retrieval results is observed when $\mathrm{Var}\,(A_s)$ becomes too large. This bifurcation happens when $\mathrm{Var}\,(A_s)$ is somewhere between 10^{-6} and 10^{-4}, varying slightly per scene. Whenever this bifurcation point is passed, a new minimum is attained, or convergence is lost.
- The new minimum that is retrieved after the bifurcation, is the unrealistic solution retrieved in the previous section.

This experiment shows that in order to have a realistic retrieval solution, we need to constrain the surface albedo's variance to a value lower than 10^{-6} around the true prior value. Thus, we need to know the surface albedo with a standard error smaller than 10^{-3}. In reality, we expect to estimate the surface albedo with an error of around $2 \cdot 10^{-2}$, see [20].

8.4 Discussion

We have discovered that the surface albedo plays a big role in the meaningfulness of our retrievals. Whenever the surface albedo is allowed too much freedom, in the optimal estimation sense, a bifurcation occurs, and retrieval results may become unrealistic. Especially for profiles that have aerosol that is mostly contained within the lower part of the atmosphere, near the surface, we see that unrealistically high mid pressures are retrieved. To improve the algorithm, we outline a few options.

First, one could decide not to fit the surface albedo altogether, and keep it as a model parameter. Although this might introduce other (potentially equally problematic) errors in the retrieval and/or convergence issues, it is at least guaranteed that the particular surface albedo related bifurcation does not occur.

Second, a different parameterization might be more useful. We see that in the sea scenes, the surface albedo takes over all the contribution to the top of atmosphere radiance from the aerosol near the surface. Since we typically find aerosol near the surface, a potential alternative parameterization may include a fixed aerosol layer near the surface, see Figure 8.5. Using such a parameterization might prevent the surface from taking over. Then, in addition to the fixed layer on the surface, another aerosol layer that is free to move might be used to capture elevated aerosol contributions. Research is needed to investigate whether the O_2 A band contains enough information to fit these two layers simultaneously, and if this parameterization is feasible.

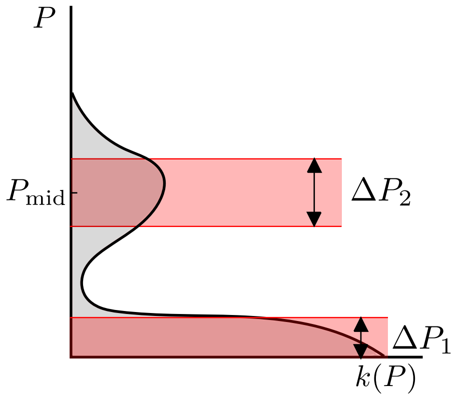

FIGURE 8.5: Schematic drawing of a true aerosol profile (gray) along with a potential new parameterization that accommodates for boundary layer aerosol (red). Here, P is the pressure, $k(P)$ is the aerosol extinction at pressure P, ΔP_1 is the pressure thickness of an aerosol layer fixed on the surface, and ΔP_2 is the pressure thicknes of an elevated aerosol layers at mid pressure P_{mid}, which is free to move.

Last, if the default Aerosol Layer Height algorithm remains the same, more research is needed to investigate the influence of errors in other parameters to the results presented here. In this research, we assumed that we know all model parameters without error, which is obviously false. Additional extensions like heterogeneous aerosol properties are also of interest.

Chapter 9

Conclusion

For our first retrieval experiment (see chapter 3), we developed eight aerosol scenes. These scenes are constructed to be representative of a realistic aerosol profile. For these typical scenes, we simulated Aerosol Layer Height retrievals. In these retrieval simulations, we did not include the surface albedo in the state vector. The simulations showed that the retrieval of Aerosol Layer Height is generally stable, and yields values that are somewhere inside the aerosol extinction profile. We conclude that this value can probably be seen as a centroid of the aerosol profile.

To better understand the retrieved height parameter, we first had to gain more knowledge about radiative transfer, via the radiative transfer equation. We introduced the radiative transfer equation and related concepts in chapters 4 and 5.

In chapter 6, we constructed a single scattering approximation to the radiative transfer equation. We also developed semi-analytic derivatives to the top of atmosphere radiance with respect to the number density of aerosol at a specific height in the atmosphere. This approximation allowed us to study radiative transfer using analytic and semi-analytic expressions, which are easy to compute and interpret, as opposed to complex multiple scattering descriptions.

We saw that the single scattering approximation is accurate inside the strong absorption parts of the O_2 A band. Both the top of atmosphere radiance and semi-analytic derivatives are approximated accurately there. This means that a low order of scattering approximation is suitable for optimization of the radiative transfer code of the Aerosol Layer Height algorithm, inside the strong absorption parts of the O_2 A band.

In chapter 7, we constructed three centroid methods to compare against the retrieved Aerosol Layer Height. The first centroid method was a simple weighted average of the aerosol extinction profile. The other two methods also accounted for the measurement's sensitivity to aerosol at a specific altitude. The sensitivities were determined using the derivatives of the measured top of atmosphere radiance with respect to the aerosol number density. The first derivative method used multiple scattering derivatives, while the second used the derivatives of the single scattering approximation.

All three centroid methods showed good agreement with the retrieved Aerosol Layer Height. Again, this is more motivation that we can interpret the retrieved Aerosol Layer Height as the centroid of the aerosol profile. Furthermore, it also means that we do not need to perform complex retrieval simulations to find a representative aerosol height parameter, as the weighted averages also suffice. This can be used for large scale validation studies. More research is needed to investigate whether these arguments still hold for a larger dataset, such that we have a higher statistical power. Furthermore, it is also interesting to investigate if a particular centroid method is preferred.

In chapter 8, we investigated whether our previous results could be extended to the default Aersol Layer Height algorithm setting, which also includes the surface albedo in its state vector. We repeated the retrieval experiment of chapter 3, but this time we used the default Aerosol Layer Height algorithm setting. This had various interesting consequences. First, the convergence and the stability of the algorithm deteriorated. Second, the retrieval now yielded unrealistic results, with a retrieved Aerosol Layer Height far above the actual aerosol profile. These solutions can no longer be interpreted as centroids of the profile.

In a third retrieval experiment, we investigated how accurately we need to estimate the surface albedo in order to maintain realistic results. Notable results were the following. For small values of the variance of the surface albedo, $\mathrm{Var}\left(A_s\right)$, retrieval results are consistent with the retrievals where we did not fit the surface albedo. We can interpret these results. However, if $\mathrm{Var}\left(A_s\right)$ is large, other (unrealistic) results are retrieved. We saw that there is a bifurcation as $\mathrm{Var}\left(A_s\right)$ increases to a value somewhere between 10^{-6} and 10^{-4}. When this bifurcation point is passed either a new minimum is attained, or convergence is lost. When a new minimum is attained, this is often an unrealistic state.

Thus, we saw that, in order to guarantee results that we can interpret as a centroid of the aerosol profile, we need a very accurate estimate of the surface albedo. This level of accuracy is hardly reachable. Therefore, other options need to be considered to avoid this problem and more research is needed.

Appendix A

Lebesgue Integration Theorems

In this work, several convergence theorems from Lebesgue integration theory are used. In this appendix, we supply these theorems and their assumptions. The theorems have been taken from [35] and, for easy reference, we will use the same numbering. Note that the integrals presented here are Lebesgue integrals.

Theorem 4.13 (Monotone Convergence Theorem)

If $\{f_n\}_{n\in\mathbb{N}}$ is a sequence of non-negative measurable functions, and $\{f_n(x) : n \geq 1\}$ increases monotonically to $f(x)$ for each $x \in E$ (measurable), i.e. $f_n \uparrow f$ pointwise, then

$$\lim_{n\to\infty} \int_E f_n(x)\mathrm{d}m = \int_E f\mathrm{d}m. \tag{A.1}$$

Theorem 4.26 (Dominated Convergence Theorem)

Suppose E is measurable. Let $\{f_n\}_{n\in\mathbb{N}}$ be a sequence of measurable functions such that $|f_n| \leq g$ almost everywhere on E for all $n \geq 1$, where g is integrable over E. If $f = \lim_{n\to\infty} f_n$ then f is integrable over E and

$$\lim_{n\to\infty} \int_E f_n(x)\mathrm{d}m = \int_E f\mathrm{d}m. \tag{A.2}$$

Theorem 4.33 (ii)

Riemann-integrable functions on $[a, b]$ are integrable with respect to Lebesgue measure on $[a, b]$ and the integrals are the same.

Appendix B

Multiple Scattering Derivatives with DISAMAR

Here, we describe how we can obtain semi-analytic derivatives of the top of atmosphere radiance using DISAMAR. This allows us to find derivatives in case of multiple scattering and a reflective surface.

Consider some atmosphere and cut it in two at the altitude at which we want to add aerosol, say z. We then obtain a top and bottom part of the atmosphere, and the top of atmosphere radiance belonging to light scattered from these combined parts of the atmosphere is denoted as $I_{\text{Top+Bot}}$.

Now, between these two half-atmospheres, we add a thin atmospheric layer of width $\mathrm{d}z$. This atmospheric layer contains both molecules and aerosol and has optical thickness $k^{\text{ext}}(z)\mathrm{d}z$. Denote the top of atmosphere radiance radiance corresponding to this new complete atmosphere as $I_{\text{Top+Thin+Bot}}$. We can then derive an expression for how the radiance changes when particles are added to the atmosphere in a thin layer with thickness $\mathrm{d}z$ located at an altitude z by looking at the difference quotient, i.e.

$$\frac{\mathrm{d}I}{\mathrm{d}z}(z) := \frac{I_{\text{Top+Thin+Bot}} - I_{\text{Top+Bot}}}{\mathrm{d}z}. \tag{B.1}$$

Now, we can take the derivative with respect to the scattering and absorption coefficients of the thin layer to obtain the derivatives $\frac{\mathrm{d}^2 I}{\mathrm{d}k^{\text{sca}}\mathrm{d}z}(z)$ and $\frac{\mathrm{d}^2 I}{\mathrm{d}k^{\text{abs}}\mathrm{d}z}(z)$. DISAMAR computes these derivatives internally using semi-analytic expressions (semi-analytic, because of the non-infinitesimal nature of the thin layer, like before).

The previous derivatives with respect to the absorption and scattering coefficients can be extracted from DISAMAR and can be used to find derivatives with respect to other properties, say x, using the chain rule:

$$\frac{\mathrm{d}^2 I}{\mathrm{d}x \mathrm{d}z}(z) = \frac{\mathrm{d}^2 I}{\mathrm{d}k^{\mathrm{sca}} \mathrm{d}z} \frac{\mathrm{d}k^{\mathrm{sca}}}{\mathrm{d}x} + \frac{\mathrm{d}^2 I}{\mathrm{d}k^{\mathrm{abs}} \mathrm{d}z} \frac{\mathrm{d}k^{\mathrm{abs}}}{\mathrm{d}x}. \tag{B.2}$$

In case of the derivative with respect to the aerosol number density, we obtain

$$\frac{\mathrm{d}^2 I}{\mathrm{d}n_{\mathrm{aer}} \mathrm{d}z}(z) = \sigma_{\mathrm{aer}}^{\mathrm{sca}} \frac{\mathrm{d}^2 I}{\mathrm{d}k^{\mathrm{sca}} \mathrm{d}z} + \sigma_{\mathrm{aer}}^{\mathrm{abs}} \frac{\mathrm{d}^2 I}{\mathrm{d}k^{\mathrm{abs}} \mathrm{d}z}. \tag{B.3}$$

This monochromatic derivative can be convolved with the slit function to obtain the derivative of the measured radiance, which we write as $\frac{\mathrm{d}^2 \hat{I}}{\mathrm{d}n_{\mathrm{aer}} \mathrm{d}z}$.

Appendix C

Model Atmosphere Properties

In this appendix we present the mid-latitude summer profile and the physical constants used for the modeling of the atmosphere, as discussed in chapter 5.

Constant Name	Symbol	Value	Units
Avogadro's constant	N_A	6.0221413×10^{23}	mol^{-1}
Specific gas constant of air	R_{specific}	287.058	$\mathrm{J\ kg^{-1}\ K^{-1}}$
Reference number density of air at 288.15 K and 1013.25 hPa	n_{ref}	2.5468993×10^{25}	molecules m^{-3}
Depolarization factor	$\delta(\lambda)$	Function. See [23].	-
Refractive index of air	$N(\lambda)$	Function. See [24].	-
Molar mass of dry air	m_{air}	0.02897	$\mathrm{kg\ mol}^{-1}$
Mixing ratio of oxygen in dry air	r_{mix}	0.2946	-

Table C.1: List of physical constants used for modeling the Rayleigh atmosphere.

Alt. (km)	Press. (hPa)	Temp. (K)	Alt. (km)	Press. (hPa)	Temp. (K)
0	1013	294.20	23	37.6	222.80
1	902	289.70	24	32.2	223.90
2	802	285.20	25	27.7	225.10
3	710	279.20	27.50	19.07	228.45
4	628	273.20	30	13.2	233.70
5	554	267.20	32.50	9.3	239.00
6	487	261.20	35	6.52	245.20
7	426	254.70	37.50	4.64	251.30
8	372	248.20	40	3.33	257.50
9	324	241.70	42.50	2.41	263.70
10	281	235.30	45	1.76	269.90
11	243	228.80	47.50	1.29	275.20
12	209	222.30	50	0.951	275.70
13	179	215.80	55	0.515	269.30
14	153	215.70	60	0.272	257.10
15	130	215.70	65	0.139	240.10
16	111	215.70	70	0.067	218.10
17	95	215.70	75	0.03	196.10
18	81.2	216.80	80	0.012	174.10
19	69.5	217.90	85	0.00448	165.10
20	59.5	219.20	90	0.00164	165.00
21	51	220.40	95	0.000625	178.30
22	43.7	221.60	100	0.000258	190.50

Table C.2: The Mid-Latitude Summer profile, taken from [27]. We present the altitude, pressure and temperature.

Appendix D

List of Symbols

Here, we present a list of common symbols used throughout the text. We also list their meaning and their units.

Symbol	Meaning	Unit
$\boldsymbol{y}$	Measurement vector	
$\boldsymbol{x}$	State vector	
$\boldsymbol{b}$	Parameter vector	
$\boldsymbol{\epsilon}$	Measurement error vector	
$\boldsymbol{F}$	Forward Model	
$\boldsymbol{\Sigma_\epsilon}$	Covariance matrix of measurement errors	
$\boldsymbol{\Sigma_a}$	Covariance matrix of prior state	
P_{mid}	Mid pressure of aerosol layer	hPa
ΔP	Pressure thickness of aerosol layer	hPa
I	Radiance	$\frac{\text{photons}}{\text{m}^2\text{ nm s sr}}$
λ	Wavelength	nm
s	Path coordinate	m
k^{ext}	Extinction coefficient	m^{-1}
k^{sca}	Scattering coefficient	m^{-1}
k^{abs}	Absorption coefficient	m^{-1}
σ^{ext}	Extinction cross section	$\frac{\text{m}^2}{\text{molecule}}$
σ^{sca}	Scattering cross section	$\frac{\text{m}^2}{\text{molecule}}$
σ^{abs}	Absorption cross section	$\frac{\text{m}^2}{\text{molecule}}$
n	Number density	$\frac{\text{molecule}}{\text{m}^3}$
j	Source coefficient	$\frac{\text{photons}}{\text{nm s sr}}$
J	Source function	$\frac{\text{photons}}{\text{m}^2\text{ nm s sr}}$

Continued on next page

Continued from previous page

z	Altitude	m
θ	Zenith angle	deg
ϕ	Azimuth angle	deg
θ_0	Solar zenith angle	deg
ϕ_0	Solar azimuth angle	deg
τ	Optical depth	-
τ^*	Optical thickness	-
u	Direction cosine	-
μ	Absolute value of direction cosine	-
μ_0	Absolute value of solar direction cosine	-
P	Phase function	sr^{-1}
ω	Single scattering albedo	-
E_0	Solar irradiance	$\frac{\text{photons}}{\text{m}^2\ \text{nm s}}$
A_S	Surface albedo	-
S_a	Single scattering source term	$\frac{\text{photons}}{\text{m}^2\ \text{nm s sr}}$
S_b	Single scattering boundary source term	$\frac{\text{photons}}{\text{m}^2\ \text{nm s sr}}$
$\hat{I}$	Measured radiance	$\frac{\text{photons}}{\text{m}^2\ \text{nm s sr}}$
S	Instrument spectral response function	-
η	Perturbation in number density	$\frac{\text{molecule}}{\text{m}^3}$
C	Constant used for derivatives	$\frac{\text{photons}}{\text{m}^2\ \text{nm s}}$
M	Geometric airmass factor	-
$\frac{\delta^2 I}{\delta n \delta z}$	Single scattering derivative	$\frac{\text{photons}}{\text{nm s sr}}$
$\frac{\text{d}^2 I}{\text{d}n\text{d}z}$	Multiple scattering derivative	$\frac{\text{photons}}{\text{nm s sr}}$
$\mathcal{Z}$	Centroid	m

TABLE D.1: List of common symbols used throughout the text.

Appendix E

Abbreviations

Here, we present a list of all abbreviations and their meanings used throughout the text.

Acronym	**W**hat it **S**tands **F**or
CALIOP	**C**loud-**A**erosol **Li**dar with **O**rthogonal **P**olarization
CALIPSO	**C**loud-**A**erosol **L**idar and **I**nfrared **P**athfinder **S**atellite **O**bservations
CAT	**C**entral **At**lantic
CEU	**C**entral **Eu**rope
DCT	**D**ominated **C**onvergence **T**heorem
DD	**D**esert **D**ust
DISAMAR	**D**etermining **I**nstrument **S**pecifications and **A**nalyzing **M**ethods for **A**tmospheric **R**etrieval
ECI	**E**ast **C**hina **I**ndustry
ESA	**E**uropean **S**pace **A**gency
FWHM	**F**ull **W**idth at **H**alf-**M**aximum
FRESCO	**F**ast **R**etrieval **S**cheme for **C**louds from the **O**xygen A band
HG phase function	**H**enyey-**G**reenstein phase function
KNMI	**K**oninklijk **N**ederlands **M**eteorologisch **I**nstituut
LABOS	**La**yer **B**ased **O**rders of **S**cattering
LIVAS	**Li**dar Climatology of **V**ertical **A**erosol **S**tructure for Space-Based Lidar Simulation Studies
MCT	**M**onotone **C**onvergence **T**heorem
NAD	**N**orth **A**frican **D**esert
NWP	**N**orth **W**est **P**acific
OMI	**O**zone **M**onitoring **I**nstrument
SA	**S**trongly **A**bsorbing
SAL	**S**outh **A**frican **L**and
SAT	**S**outh **At**lantic
SPA	**S**outh **Pa**cific
SS	**S**ea **S**alt
TROPOMI	**Tropo**spheric **M**onitoring **I**nstrument
VU	**V**rije **U**niversiteit Amsterdam
WA	**W**eakly **A**bsorbing

Table E.1: Table listing the abbreviations and their meaning used throughout the text.

Appendix F

List of Figures

Bibliography

[1] World Health Organization. *Burden of disease from household air pollution for 2012.* Downloaded from `http://www.who.int/phe/health_topics/outdoorair/databases/FINAL_HAP_AAP_BoD_24March2014.pdf` on April 9th 2014, released: March 2014.

[2] International Air Transport Association. *IATA economic briefing - the impact of Eyjafjallajökull's volcanic ash plume.* Downloaded from `http://www.iata.org/whatwedo/Documents/economics/Volcanic-Ash-Plume-May2010.pdf` on April 9th 2014, released: May 2010.

[3] Matthias et al. *The ash dispersion over europe during the Eyjafjallajökull eruption - comparison of CMAQ simulations to remote sensing and air-borne in-situ observations.* Atmospheric Environment, 48:184–194, March 2012.

[4] Pappalardo et al. *EARLINET: towards an advanced Sustainable European aerosol lidar network.* Atmospheric Measurement Techniques Discussions, 7:2929–2980, 2014.

[5] Winker et al. *The global 3-D distribution of tropospheric aerosols as characterized by CALIOP.* Atmospheric Chemistry and Physics, 13:3345–3361, March 2013.

[6] A.F.J. Sanders and J.F. de Haan. *Retrieval of aerosol parameters from the oxygen A band in the presence of chlorophyll fluorescense.* Atmospheric Measurement Techniques, 6(10):2725–2740, October 2013.

[7] A.F.J. Sanders and J.F. de Haan. *TROPOMI ATBD of the Aerosol Layer Height product.* KNMI, June 2013.

[8] Veefkind et al. *TROPOMI on the ESA Sentinel-5 Precursor: A GMES mission for global observations of the atmospheric composition for climate, air quality and ozone layer applications.* Remote Sensing of Environment, 120:70–83, February 2012.

[9] Koelemeijer et al. *A fast method for retrieval of cloud parameters using oxygen A band measurements from the Global Ozone Monitoring Experiment.* Journal of Geophysical Research, 106:3475–3490, February 2001.

[10] V.V. Rozanov and A.A. Kokhanovsky. *Seminanalytical cloud retrieval algorithm as applied to the cloud top altitude and the cloud geometrical thickness determination from top-of-atmosphere reflectance measurements in the oxygen A band.* Journal of Geophysical Research, 109, 2004.

[11] Menzel et al. *MODIS Global Cloud-Top Pressure and Amount Estimation: Algorithm Description and Results.* American Meteorological Society, 47:1175–1198, April 2008.

[12] Joiner et al. *Fast simulators for satelllite cloud optical centroid pressure retrievals; evaluation of OMI cloud retrievals.* Atmospheric Measurement Techniques, pages 529–545, March 2012.

[13] Gabella et al. *Retrieval of aerosol profile variations in the visible and near infrared: theory and application of the single-scattering approach.* Applied Optics, 36:1328–1336, February 1997.

[14] J.F. de Haan. *DISAMAR: Determining Instrument Specifications and Analyzing Methods for Atmospheric Retrieval, Algorithm description and background information.* KNMI, May 2011.

[15] J.F. de Haan, P.B. Bosma, and J.W. Hovenier. *The adding method for multiple scattering calculations of polarized light.* Astronomy and Astrophysics, 183(2):371–391, September 1987.

[16] C.D. Rodgers. *Inverse methods for atmoshperic sounding: theory and practice.* Series on Atmoshperic, Ocean and Planetary Physics - Vol. 2. World Scientific, 2000.

[17] G.E. Thomas and K. Stamnes. *Radiative Transfer in the Atmoshpere and Ocean.* Cambridge Atmospheric and Space Science Series. Cambridge University Press, 2002.

[18] K. Liou. *An Introduction to Atmospheric Radiation.* International Geophysics Series. Academic Press, Inc., 1980.

[19] K. Chance and R.L. Kurucz. *An improved high-resolution solar reference spectrum for earth's atmosphere measurements in the ultraviolet, visible and near infrared.* Journal of Quantitative Spectroscopy and Radiative Transfer, 111:1289–1295, January 2010.

[20] Koelemeijer et al. *A database of spectral surface reflectivity in the range 335-772 nm derived from 5.5 years of GOME observations.* Journal of Geophysical Research, 108, January 2003.

[21] J. Strutt. *On the transmission of light through an atmosphere containing small particles in suspension, and on the origin of the blue of the sky.* Philosophical Magazine, 47:375–394, 1899.

[22] J.D. Jackson. *Classical Electrodynamics.* Wiley, 2nd edition, 1975.

[23] N.J. Bridge and A.D. Buckingham. *The Polarization of Laser Light Scattered by Gases.* Proceedings of The Royal Society A: Mathematical, Physical and Engineering Sciences, December 1966.

[24] E.R. Peck and K. Reeder. *Dispersion of air.* Journal of the Optical Society of America, 62, 1972.

[25] C. Boulet H. Tran and J.-M. Hartmann. *Line mixing and collision-induced absorption by oxygen in the A band: Laboratory measurements, model, and tools for atmospheric spectra computations.* Journal of Geophysical Research, 111, August 2006.

[26] H. Tran and J.-M. Hartmann. *An improved O2 A band absorption model and its consequences for retrievals of photon paths and surface pressure.* Journal of Geophysical Research, 113, September 2008.

[27] Anderson et al. *AFGL Atmoshperic Constituent Profiles (0-120km).* Environmental Research Papers, May 1986.

[28] R. Goody. *Principles of Atmospheric Physics and Chemistry.* Oxford University Press, 1995.

[29] Dubovik et al. *Variability of Absorption and Optical Properties of Key Aerosol Tyes Observed in Worldwide Locations.* Journal of The Atmospheric Sciences, 59:590–608, May 2001.

[30] He et al. *Aerosol optical peroperties retrieved from Sun photometer measurements over Shanghai, China.* Journal of Geophysical Research, 117, August 2012.

[31] Holzer-Popp et al. *Aerosol Retrieval Experiments in the ESA Aerosol_CCI Project.* Atmospheric Measurement Techniques, 6:1919–1957, August 2013.

[32] W.A. de Rooij and C.A.A.H. van der Stap. *Expansion of Mie scattering matrices in generalized spherical functions.* Astronomy and Astrophysics, 131:237–248, October 1983.

[33] P.C. Waterman. *Matrix formulation of electromagnetic scattering.* Proceedings of the IEEE, 53:805–812, August 1965.

[34] V. Pavlou and I. Metaxa. *LIVAS - Lidar Climatology of Vertical Aerosol Structure for Space-Based Lidar Simulation Studies.* The European Space Research and Technology Centre, August 2013. ESTEC Contract No. 4000104106/11/NL/FF/fk.

[35] M. Capiński and E. Kopp. *Measure, Integral and Probability.* Springer Undergraduate Mathematics Series. Springer, 2nd edition, 2005.

A complete list of all KNMI-publications (1854 – present) can be found on our website

www.knmi.nl/knmi-library/knmipub_en.html

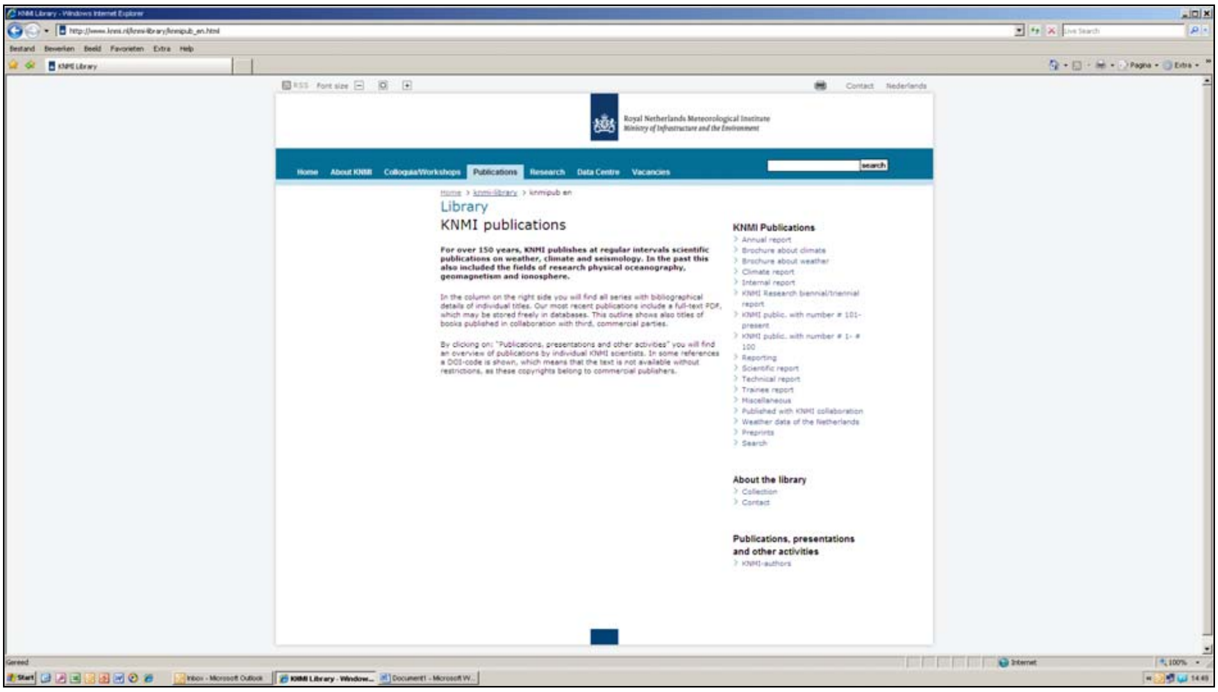

Library

KNMI publications

For over 150 years, KNMI publishes at regular intervals scientific publications on weather, climate and seismology. In the past this also included the fields of research physical oceanography, geomagnetism and ionosphere.

In the column on the right side you will find all series with bibliographical details of individual titles. Our most recent publications include a full-text PDF, which may be stored freely in databases. This outline shows also titles of books published in collaboration with third, commercial parties.

By clicking on: "Publications, presentations and other activities" you will find an overview of publications by individual KNMI scientists. In some references a DOI-code is shown, which means that the text is not available without restrictions, as these copyrights belong to commercial publishers.

KNMI Publications
- Annual report
- Brochure about climate
- Brochure about weather
- Climate report
- Internal report
- KNMI Research biennial/triennial report
- KNMI public. with number # 101-present
- KNMI public. with number # 1- # 100
- Reporting
- Scientific report
- Technical report
- Trainee report
- Miscellaneous
- Published with KNMI collaboration
- Weather data of the Netherlands
- Preprints
- Search

About the library
- Collection
- Contact

Publications, presentations and other activities
- KNMI-authors

The most recent reports are available as a PDF on this site.